Julius-Maximilians-
UNIVERSITÄT
WÜRZBURG

Functional and Microstructural MRI of the Human Brain Revealing a Cerebral Network Processing the Age of Faces

Dissertation zur Erlangung des
naturwissenschaftlichen Doktorgrades
der Julius-Maximilians-Universität Würzburg

vorgelegt von
Dipl. Biol. **György Ádám Homola**
aus Budapest

Würzburg 2011

Die vorliegende Arbeit wurde in der Zeit von Mai 2006 bis Dezember 2010 in der Abteilung für Neuroradiologie des Institutes für Röntgendiagnostik des Universitätsklinikums Würzburg bei Prof. Dr. L. Solymosi unter Anleitung von Prof. Dr. L. Solymosi und Dr. Andreas J. Bartsch angefertigt.

Eingereicht am: **24. März 2011**

Mitglieder der **Promotionskommission**:

Vorsitzender: **Prof. Dr. M. Engstler** (vom Dekan beauftragt)

1. Gutachter: **Prof. Dr. L. Solymosi**

2. Gutachter: **Prof. Dr. W. Rössler**

Tag des Promotionskolloquiums: **18. Mai 2011**

Doktorurkunde ausgehändigt am: ……..

"People remain what they are even if their faces fall apart."

Bertolt Brecht

"It has been said that a pretty face is a passport. But it's not, it's a visa, and it runs out fast."

Julie Burchill

"Youth has no age."

Pablo Picasso

Table of Contents

List of Chapters

List of Figures

List of Tables

I. Acknowledgements

Without assistance, cooperation and continuous support of many people the completion of this doctoral thesis would not have been possible.

Firstly, I am deeply indebted to Professor L. Solymosi under whose auspices the entire work was carried out. Both Professor L. Solymosi and Dr. Andreas J. Bartsch deserve my gratitude for their dedicated supervision and support over the years. The expertise of Dr. Bartsch was invaluable in assisting the design of the study, the data acquisition and the analyses carried out.

For auxiliary assistance in data analysis and interpretation as well as constructive reviewing I wish to thank Saad Jbabdi and Christian F. Beckmann.

Furthermore, I am grateful for inspiration and expedient notes from E.K. Warrington, just as T.E. Behrens, A. Biller, B. Fischl, D. Greve, M. Hanke, M. Jenkinson, D. Dierker and S.M. Smith for their substantial advice.

Additionally, I'd like to thank Professor W. Rössler for being available as auditor and advisor for the Faculty of Biology at the University of Würzburg. The entire Department of Neuroradiology Würzburg made it possible to carry out the study and the staff provided essential support.

Last but not least I am deeply grateful to my family, especially to my parents.

II. Summary

Although age is one of the most salient and fundamental aspects of human faces, its processing in the brain has not yet been studied by any neuroimaging experiment. Automatic assessment of temporal changes across faces is a prerequisite to identifying persons over their life-span, and age per se is of biological and social relevance. Using a combination of evocative face morphs controlled for global optical flow and functional magnetic resonance imaging (fMRI), we segregate two areas that process changes of facial age in both hemispheres. These areas extend beyond the previously established face-sensitive network and are centered on the posterior inferior temporal sulcus (pITS) and the posterior angular gyrus (pANG), an evolutionarily new formation of the human brain. Using probabilistic tractography and by calculating spatial cross-correlations as well as creating minimum intersection maps between activation and connectivity patterns we demonstrate a hitherto unrecognized link between structure and function in the human brain on the basis of cognitive age processing.

According to our results, implicit age processing involves the inferior temporal sulci and is, at the same time, closely tied to quantity decoding by the presumed neural systems devoted to magnitudes in the human parietal lobes. The ventral portion of Wernicke's largely forgotten perpendicular association fasciculus is shown not only to interconnect these two areas but to relate to their activations, i.e. to transmit age-relevant information. In particular, post-hoc age-rating competence is shown to be associated with high response levels in the left angular gyrus. Cortical activation

patterns related to changes of facial age differ from those previously elicited by other fixed as well as changeable face aspects such as gender (used for comparison), ethnicity and identity as well as eye gaze or facial expressions. We argue that this may be due to the fact that individual changes of facial age occur ontogenetically, unlike the instant changes of gaze direction or expressive content in faces that can be "mirrored" and require constant cognitive monitoring to follow.

Discussing the ample evidence for distinct representations of quantitative age as opposed to categorical gender varied over continuous androgyny levels, we suggest that particular face-sensitive regions interact with additional object-unselective quantification modules to obtain individual estimates of facial age.

III. Zusammenfassung

Obwohl das Alter eines der markantesten und grundlegendsten Aspekte menschlicher Gesichter darstellt, hat man die Verarbeitung im Gehirn noch nicht durch ein funktionell bildgebendes Verfahren untersucht und mit strukturellen Leitungsbahnen in Verbindung gebracht. Die automatische Bewertung der altersbedingten Veränderungen in Gesichtern ist eine Voraussetzung für die Identifizierung von Personen über ihre gesamte Lebenszeit, und das Lebensalter an sich ist von biologischer und sozialer Relevanz. In dieser Dissertation wird die funktionelle Kernspintomographie (fMRI) mit eindrucksvollen Gesichtsmorphs kombiniert, welche auf sichtbare Bewegung im gesamten Bild kontrolliert wurden. Hierdurch werden zwei Bereiche auf beiden Hemisphären isoliert, welche die Veränderungen des Alters von Gesichtern gemeinsam und automatisch verarbeiten. Diese Areale reichen über das zuvor etablierte gesichtssensible Netzwerk hinaus und zentrieren sich auf den hinteren inferio-temporalen Sulcus (pITS) und den hinteren angulären Gyrus (pANG), eine evolutionäre Neubildung des menschlichen Gehirns. Mit Hilfe der probabilistischen Traktographie diffusiongewichteter MRT-Daten und der Berechnung räumlicher Kreuzkorrelationen sowie der Erstellung von Minimum Intersection Maps zwischen Aktivierungs- und Konnektivitätsmustern wird ein bisher unerkannter Zusammenhang zwischen Struktur und Funktion des menschlichen Gehirns anhand der kognitiven Altersverarbeitung aufgezeigt.

Unseren Ergebnissen zufolge wird der inferiore temporale Sulcus in die implizite Altersverarbeitung einbezogen und gleichzeitig eng mit der Mengendekodierung

verknüpft, welche in den vermutlich Größenabschätzungen gewidmeten neuronalen Systemen im Scheitellappen des menschlichen Gehirns erfolgt. Es wird dargelegt, dass der ventrale Teil von Wernickes weitgehend vergessenem senkrecht verlaufendem Assoziationsbündels nicht nur diese beiden Bereiche miteinander verbindet, sondern auch mit ihren Aktivierungen in Beziehung steht, was die These stützt, dass altersrelevante Informationen tatsächlich über ihn übertragen werden. Bei der nachträglichen Alterseinschätzung der Gesichter zeigt sich, dass gutes Abschneiden der Versuchspersonen mit stärkeren Aktivierungen im linken angulären Gyrus einhergeht. Die kortikalen Aktivierungsmuster auf Änderungen des Gesichtsalters unterscheiden sich von jenen, die mit anderen wechselnden Gesichtsmerkmalen in Zusammenhang gebracht wurden, welche das Geschlecht (das zum Vergleich und zur Kontrolle herangezogen wurde), die Ethnizität und die personelle Identität sowie Blickrichtungen und Mimik betreffen. Es wird argumentiert, dass dies möglicherweise auf die Tatsache zurückzuführen ist, dass individuelle Änderungen des Gesichtsalters ontogenetisch auftreten, anders als beispielsweise die flüchtigen Wechsel von Blickrichtungen oder im Ausdruck in Gesichtern, welche vom Betrachter "gespiegelt" werden können und ständige Beobachtung erfordern, um kognitiv nachvollzogen werden zu können.

Damit wird erstmals die eigene Art der Wahrnehmung und Verarbeitung des quantitativen Alters im direkten Gegensatz zu kategorischem Geschlecht belegt, welches über kontinuierliche Androgyniegrade variiert: Bestimmte gesichtssensible Regionen interagieren offenbar mit zusätzlichen nicht objekt-selektiven Quantifizierungsmodulen, um das Alter eines Gesichts individuell abzuschätzen.

1. Introduction

1.1. Face processing

Identifying the neural correlates of apperceptive and associative object classification remains a fundamental challenge in cognitive neuropsychology. Investigations into the cerebral representation of different object categories are central to our current models of the ventral visual stream [**1-3**]. Face processing within the ventral visual stream is linked to distinct brain regions whose degree of specificity and selectiveness continues to be a matter of controversy and ongoing research [**4-15**]. Several studies have addressed differences and similarities in where and how faces are processed as compared to other objects [**5, 11-24**], including the non-face entity and various portions of the human body as well as face parts [**25-27**].

From these insights the fusiform face area (FFA), named after its common functional localization within the fusiform gyrus (FFG), has emerged as the most well-known face-sensitive region specialized to represent invariant visual attributes mediating identity recognition. Consequently, categorical perception of generally unchangeable facial gender has recently been associated with FFG/FFA activations during graded but static face encodings of linear sexual transitions [**28**]. However, the core system of the face-sensitive network proposed to respond also to variable face aspects reveals a broader cortical distribution, especially supported by the superior temporal sulcus, and task-dependent activations [**29-32**].

1.2. Age processing in neuroimaging

Processing the age of faces is a crucial cognitive skill. Age recognition is essential in various social contexts and to identify minors, seniors, peers, missing persons as well as suspects. Profound changes of facial age may challenge or even prevent identity recognition which otherwise is, within certain limits, age-invariant [**33**]. After initial categorical distinction between faces and other kinds of objects [**34**], the search for fixed visual attributes mediating identity recognition continues to engage the fusiform face area (FFA) [**15, 20, 24, 35**], particularly within the right fusiform gyrus (FFG) [**36**]. Gender categorization of faces has been linked to graded FFA and lateral FFG activations [**28**] but adaptation suggests more widely distributed responses to invariant cues of gender, ethnicity and identity [**37**] involving the FFG yet outside FFA as traditionally defined by face/non-face stimuli [**16**]. Changeable aspects of faces, i.e. eye gaze, lip movements and facial expression, and the face parts associated with them revealed selective cortical responses in the superior temporal sulcus (STS) [**29, 30, 32, 38-41**]. Amazingly, the processing of facial age, one of the most salient changeable face aspects, has not yet been investigated by any functional or structural neuroimaging study.

Across individuals, the age of a face is independent from its gender or ethnicity, and different identities can obviously be of the same age. Within individuals, facial aging occurs inevitably, regardless of personal gender or identity, and involves complex changes of face configuration, head shape, textural and other features [**42**]. Because judgments of age and gender need not be affected in prosopagnosia [**43, 44**], spatial

representations of facial identity, gender and age should, at some level, dissociate. However, irrespective of face identity or familiarity recognition, cases selectively agnostic for face gender but not age or vice versa have not been reported in the literature. Even though age is a quantitative and relative classifier whereas gender is primarily categorical, the latter also varies across different androgyny levels, and gender differentiation changes with age. Eye, mouth and expressive face movements, on the other hand, are volatile compared to gender and age. Therefore, we designed our study to specifically compare the processing of facial age and gender in a group of healthy individuals.

1.3. Morphing of faces

Age is extremely salient in faces but, at least for children, less than gender and ethnicity [**45**]. In order to further augment its processing, we utilize face morph animations which provide useful modulations of the age parameter: Attracting visual attention to the optical flow of such changes can be expected to enhance physiological neural responses to every attribute of the morphed object [**46**]. Possibly due to such effects, dynamic morphing has increasingly been adopted in arts and entertainment (see motion pictures such as “Terminator 2” [**47**], “The Devil's Advocate” [**48**] and “The Matrix” [**49**] or music videos such as “Black or White” [**50**] for striking realizations). For the same reason, continuous morphing seems also suited to minimize adaptation and to facilitate implicit processing without particular cognitive efforts. Static images from graded morph transitions have already been used to investigate face processing [**12, 28, 36, 37, 39, 51**] but age has either not been varied or explicitly

controlled for. Animations of continuous morphing have not yet been applied in functional neuroimaging experiments. For this study, we generate continuous face morphs introducing both age as well as gender changes (see **Figure 2.2**, **Materials and Methods** and **Appendix**) controlled for global optical flow (also see **Materials and Methods**, **Figures 2.6** and **2.7**). We use functional (fMRI) and diffusion-weighted (DWI) magnetic resonance imaging (see below) to localize and characterize the neural basis for processing the age of faces compared to their gender in the human brain.

1.4. MRI modalities

By inducing spatial gradients in a strong static magnetic field and radio frequency pulses, the spin characteristics of protons, ubiquitous in water molecules, are determined to visualize structural and functional information of organic tissue. Since the very first magnetic resonance images have been recorded [**52, 53**], the main advantages of MRI over other imaging methods, i.e. high spatial resolution and noninvasiveness, inspired researchers and vendors to improve the technology as far as making it possible to acquire complete 3D datasets of the whole brain (see **Figure 1.1A**) in a remarkably short period of time. FMRI, as a spin-off of MRI, enables us to map blood oxygenation level-dependent (BOLD) signal changes accompanying neuronal activations mainly in gray matter [**54-56**]. Given that it is necessary to record as many volumes as possible during paradigm presentation, spatial resolution has to be reduced considerably (see **Figure 1.1B**). DWI, on the other hand, is used to reveal microstructural features such as axonal fiber orientation, organization and trajectories in white matter [**57**]. By measuring directional dependence of proton motion, DWI is

sensitive to local hindrance of water diffusion [**58**]. Such a boundary is most effective perpendicular to myelinated axonal fiber tracts. Bayesian estimation of diffusion parameters is applied to compute principle diffusion directions at each voxel (see **Figure 1.1C** and **Materials and Methods**). Probabilistic tractography of DWI data utilizes this property to enable quantitative analyses of connectivity between gray matter areas [**59**].

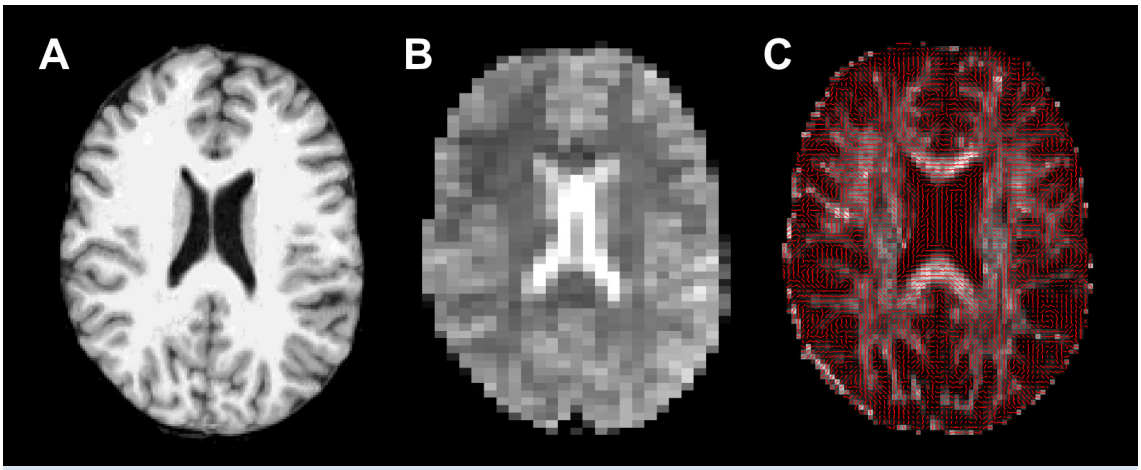

Figure 1.1: Comparison of structural, functional and microstructural MRI
(**A**) Axial view of skull stripped T1-weighted (MP-RAGE) anatomical data. (**B**) Functional (T2*-weighted BOLD) slice showing the same subject at lower resolution. (**C**) Lines at each voxel representing the principle diffusion direction overlaid on processed DWI data revealing fiber pathways by merged samples from the distribution on anisotropic volume fraction. (Also see **Materials and Methods** for technical details.)

1.5. Segmentation and surface reconstruction of the human brain

The human cerebral cortex is highly folded. It is challenging to visualize individual brains, to view functional activations in an optimal way as well as to achieve precise inter-subject transformations. The reconstruction of the cortical surface is accomplished by a complex procedure [**60**] and requires a lot of computing power

which has not been available to the scientific community until a few years ago. Accurate segmentation of white and gray matter (see **Figure 1.2A**) is essential to properly inflate, cut and flatten each hemisphere, or merely render the highly folded geometry in 3D (see **Figure 1.2B**).

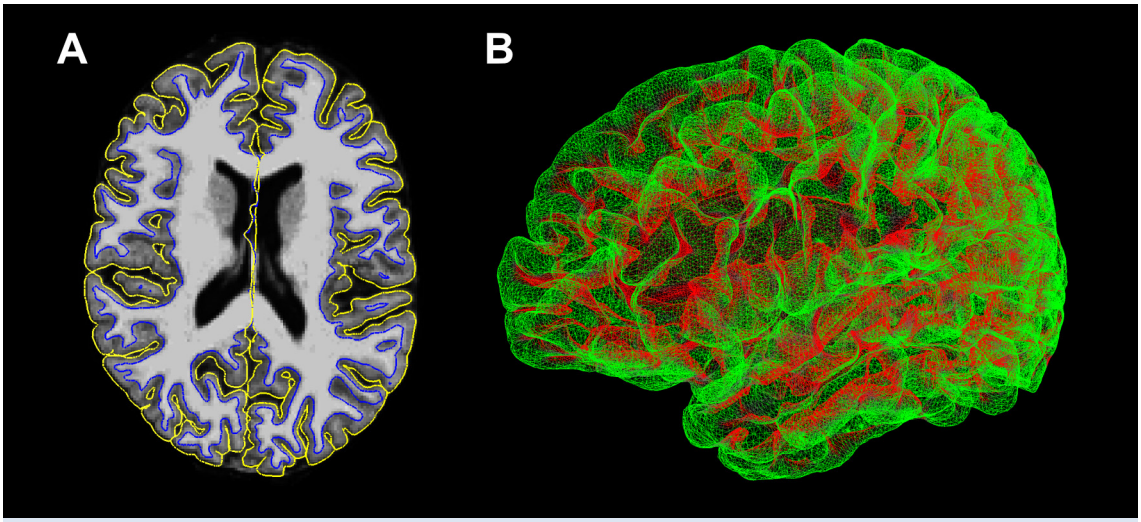

Figure 1.2: Segmented and rendered anatomical volume
(**A**) Accurate segmentation of the cerebrum into the white surface (blue line, white / gray matter boundary) and the pial surface (yellow line). (**B**) The highly folded geometry of the cortex is specified as a mesh of vertices (zoom to enlarge if possible) that can be visualized as a colored wire-frame representing the original curvature of the gyri (green) and sulci (red).

The cortical map can be transformed into a more simple but better parameterizable surface such as a sphere [**61**] in order to build a surface-based coordinate system that provides the basis for accurate subject-to-subject and subject-to-average space transformations (see **Figure 1.3** and **Materials and Methods**). Transformation from individual subject space to a common average space is indispensable for group analysis on higher level where the contrasts of parameter estimates (COPEs) and their associated variance (both based on first level general linear modeling of time series)

are concatenated and statistically merged to a valid spatial distribution of activation and deactivation probabilities (also see **Materials and Methods**).

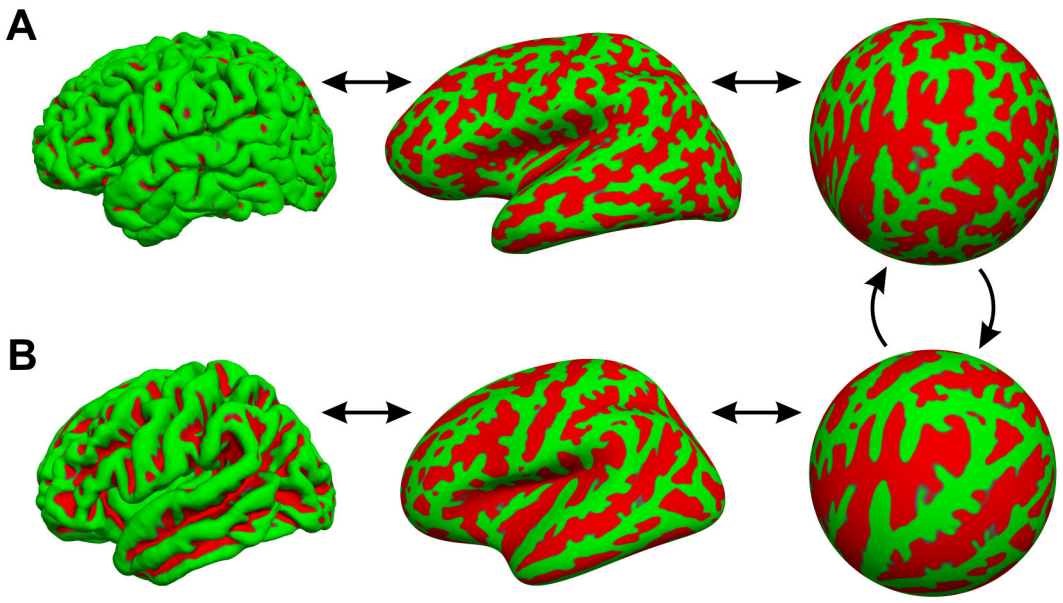

Figure 1.3: Inflation and transformation of the cortical surface
(**A**) The parameterized pial surface of the subject is inflated to a hemisphere uncovering the otherwise hidden infoldings, such as the insular cortex and the deep sulci. By utilizing a spherical surface-based coordinate system that is adapted to the folding pattern of each individual subject, the vertices are non-rigidly aligned to the average space. (**B**) The gyri (green) of the average surface appear smoother, the sulci (red) are significantly wider than of any native human cerebral surface. (Also see **Materials and Methods**.)

1.6. Primary objectives of the study

Here we combine BOLD fMRI and probabilistic tractography in a unique analysis to investigate the following: ***(I)*** Do facial age and gender transitions during morph sequences (see **Figure 2.2** and **Materials and Methods**) engage separate functional networks? ***(II)*** Are significant age-related activations evoked beyond the previously established face-sensitive network encoding fixed and changeable aspects of faces,

such as identity and eye gaze direction or emotional expression [**29-32**], i.e. in areas not traditionally linked to face processing? ***(III)*** Which of the age-responsive areas are associated with high age-rating competence? ***(IV)*** If two or more areas process changes of facial age, are these interconnected by association and / or commissural pathways? Such a structural connection between areas within and beyond the known face-sensitive network, for example, would suggest the capacity of face-responsive brain regions to recruit additional neuronal modules for age processing. However, the mere presence of such a connection is necessary but by no means sufficient to imply its functional involvement. In order to establish if age-responsive areas interact with each other directly via association and / or commissural connections, we therefore investigate the additional question: ***(V)*** Is the pattern of functional activations within age-responsive areas related to the structural connectivity between them? Utilizing surface-based minimum intersection maps (see **Materials and Methods** and **Results**) and spatial cross-correlations between functional activation probabilities and structural connectivities not hitherto reported, we examine if the activation pattern of one area is predicted by its intrinsic connectivity with another, i.e. evidence for two selected areas directly interacting with each other as connections to the latter determine activation of the former and vice versa. Gender is again used for within- and across-condition comparison. These methodological advances (minimum intersection maps, spatial cross-correlations between activation probabilities and fiber connectivities) are crucial to assess the potential impact of extracted connections on activation patterns. Thereby, we seek to further substantiate which fiber pathways are transmitting age-relevant face information.

2. Materials and Methods

2.1. Subjects

We obtained BOLD fMRI and DWI scans of 24 right-handed, healthy, white Caucasian volunteers (age range 23 to 34, mean age 26, standard deviation 3 years; 12 females) who gave written informed consent and participated in this study. The Ethics Committee of the University of Würzburg (Faculty of Medicine) approved the survey. Handedness was assessed by a variant of the Edinburgh Handedness Inventory [**62**], expanded by one eye and foot preference item [**63**]. Females were scanned between day 5 to 15 of their menstrual cycle and off any oral contraceptives.

For external validation of the tractography results, diffusion-weighted imaging (DWI) data of additional 46 right-handed healthy volunteers (age range 19 to 63, mean age 30, standard deviation 9 years; 25 females) from the Oxford Centre for Functional MRI of the Brain (FMRIB, University of Oxford) database were analyzed.

2.2. Experimental Paradigm design

Full-front photographs of 121 unfamiliar, unambiguously gendered faces of white Caucasians (age range 2 to 81, mean age 33, standard deviation 15 years; 60 females age-matched to the males; all unrouged and beardless, with eye gaze directed at the viewer, wearing no jewelry or piercings, without tattoos; rated as neutral in their expression on a 6-point visual analogue scale by all participants) were parameterized by a computerized algorithm [**64**] to a morphable three dimensional (3D) model (see

Figure 2.1) consisting of a surface mesh of editable polygons and texture materials using FaceGen Modeller [**65**] and 3ds Max [**66**].

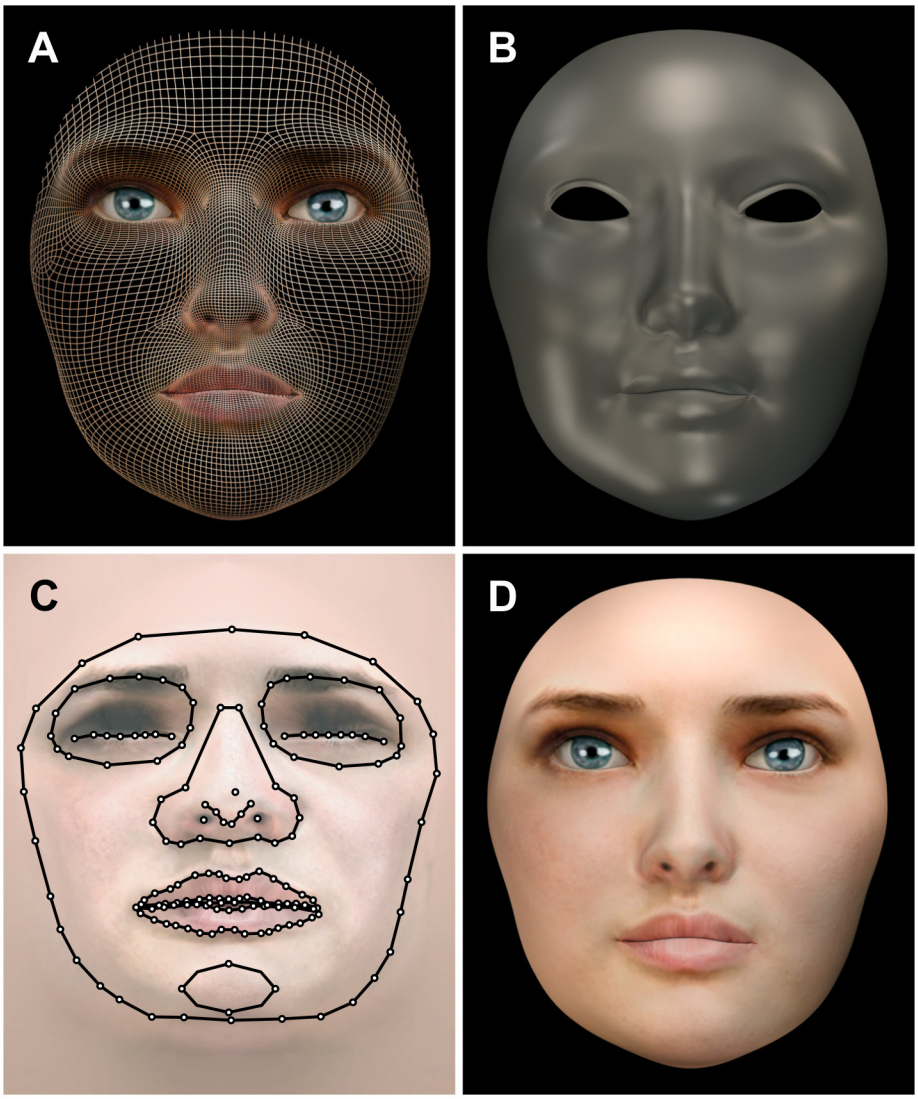

Figure 2.1: Construction of the 3D face model.
(**A**) surface mesh consisting of editable polygons, only eyes shown with texture overlay, (**B**) illuminated texture-free surface model, (**C**) flattened bitmap overlay with fiducial points to enhance texture morph consistency based on anthropological landmarks and respecting individual skin characteristics, (**D**) merged final 3D face model.

From these models (n = 120) 3D face morphs were rendered, half of them containing gender transitions further refined compared to static images applied previously [**28,**

37] (see **Figure 2.2**). To avoid rendering artifacts, landmark-based morphing by MorphMan 2000 [**67**] was chosen aligning fiducial markers arranged in 13 groups of 168 nodes to enhance texture morph consistency with respect to anthropological markers as well as individual skin characteristics (see **Figure 2.1C**). Since all face stimuli were generated by the fully morphable 3D model, intermediate virtual faces were constrained to appear as realistic as the true endpoints. Face stimuli were presented in a frontal, slightly cropped view, with ears, neck, upper parts of the forehead and hair removed (see **Figures 2.1D** and **2.2**).

Morphing transitions between two faces lasted 6 seconds (see **Figure 2.2** and **Appendix**), with an additional one-second still in-between to facilitate cognitive "segmentation" into morph pairs and to better maintain attention for the 14 minutes of paradigm presentation. Face morphs with and without gender transitions were arranged in random order. Facial age of the stimuli was continuously modulated, except for the one-second stills, with age changes being pseudo-randomized according to 10-year intervals. These morphing videos of unfamiliar faces were presented to the (n = 24) subjects. Age changes during morphing were orthogonal to gender transitions. Psychophysical changes of age and gender were modeled according to Steven's power law (see below, **Figures 2.3**, **2.4** and **2.5**). Optical flow was extracted by the Horn-Schunck method and integrated as a global confound (see below; also see **Figures 2.6** and **2.7A**). Our functional probe and modeling simultaneously engages configural and textural processing (see also **Introduction**, **Results** and **Discussion** as well as the **Appendix**), both known to be involved in categorical face processing [**7**].

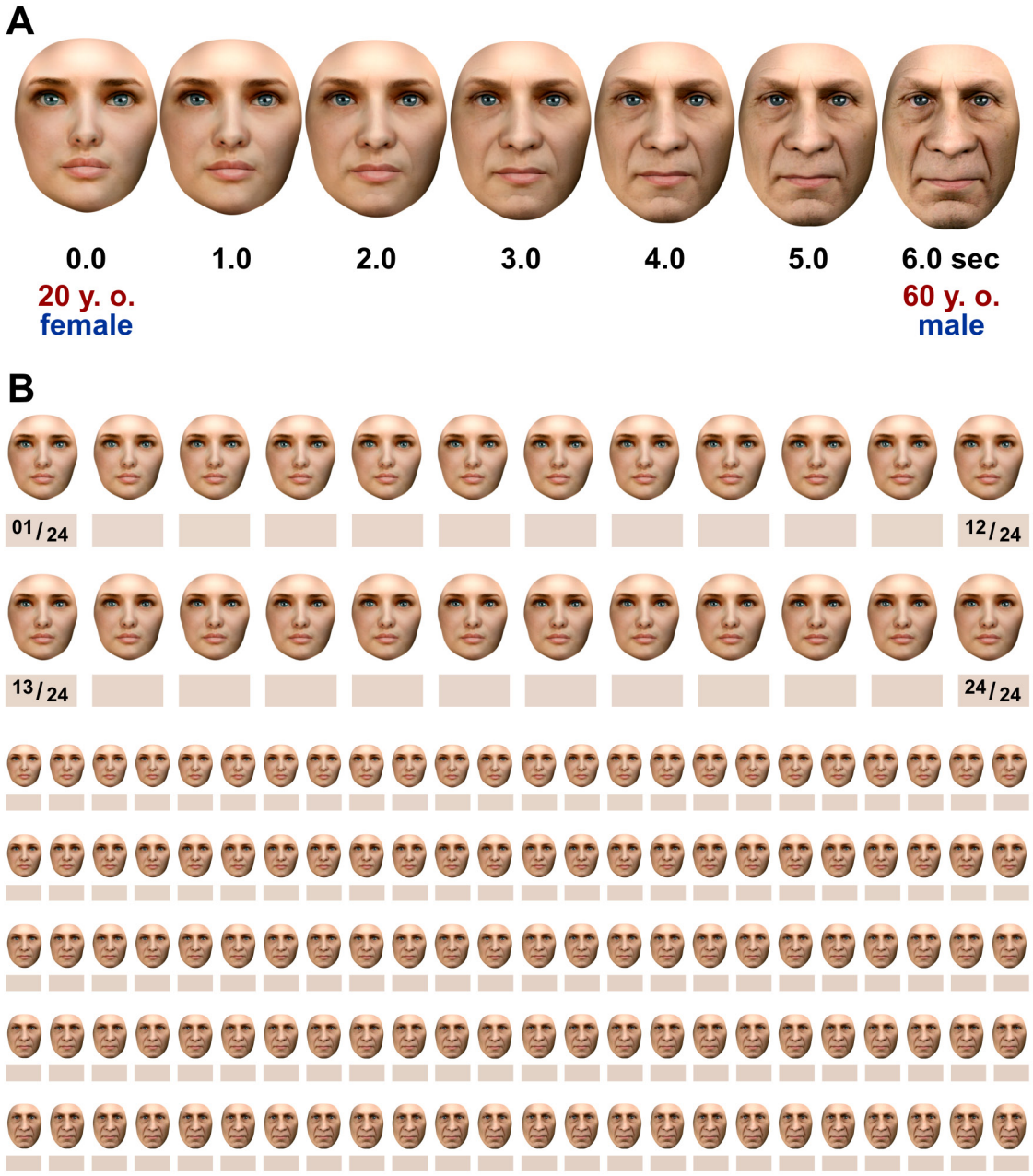

Figure 2.2: Exemplary morph video

(**A**) Key frames of a video sequence (also see **Appendix**) morphing a 20 year-old female into a 60 year-old male. Both gradual age as well as gender change is illustrated at intervals of 1 second. (**B**) Color balance of the displayed paradigm was effectively kept constant (here for every of the 144 frames of the 6 second exemplary morphing sequence) as illustrated by the average frame color boxes below the faces (with overlaid frame numbers for the first second; also see **Appendix** for technical details). Note that differences between the successive frames are subliminal when rendered at 24 fps, i.e. the morphing proceeds continuously.

2.3. Paradigm presentation and feedback

The morphing video clip was presented at 24 frames per second (fps) using a fMRI-compatible LCD screen. At the display, global luminance was controlled for and constant color channel ratios were maintained (see **Figure 2.2** and **Appendix**). Temporal synchronization between video presentation and the scanning was achieved by triggering the start of each fMRI volume externally at a minimum precision of 50 µs using MATLAB [**68**] .To sustain attention and to monitor compliance of the participating volunteers by their feedback, subjects were instructed to press a key with their right index finger whenever the target face appearance of the morphing sequence was anticipated. Speed and accuracy were not emphasized for the purpose. Key-press feedbacks to the video display were recorded by a fMRI-compatible keyboard and logged by Cogent 2000 [**69**].

2.4. MRI data acquisition

Functional and T1-weighted structural MRI data were acquired on a 3 Tesla TimTrio scanner (Siemens, Erlangen, Germany) using a 12-channel head coil. Whole brain T2*-weighted BOLD images were recorded by a single-shot gradient-echo 2D echo-planar imaging (EPI) sequence with interleaved slice acquisition (volume repetition time TR = 2400 ms; echo time TE = 30 ms; resolution 3x3x4 mm^3; 25 % interslice gap; 30 sagittal slices; flip angle FA = 90°). After discarding the four initial scans to reach global steady-state, 350 volumes acquired during visual paradigm presentation were analyzed. In order to unwarp geometric distortions of BOLD EPIs, we used gradient-echo fieldmaps (TR = 500 ms; TE1 = 4.30 ms; ΔTE = 2.46 ms; FA = 55°). In addition,

a T1-weighted 3D anatomical image using a MPRAGE sequence (TR = 1560 ms; TE = 2.26 ms; FA = 90°, resolution 1×1×1 mm^3) optimized for segmentation and surface reconstructions and, for neuroradiological screening, a T2-weighted 2D axial FLAIR sequence, both covering the entire brain, were acquired.

In order to avoid potential DWI signal-loss artefacts [**70**], we recorded whole-brain diffusion-weighted EPI volumes (60 diffusion directions isotropically distributed on a sphere at b = 1000 s/mm^2; TR = 9000 ms; TE = 97 ms ; 60 axial slices; resolution 2×2×2.5 mm^3, 20 % interslice gap) plus five volumes without diffusion weighting on a 1.5 Tesla Quantum Vision scanner (Siemens, Erlangen, Germany). For unwarping their geometric distortions, gradient-echo fieldmaps matching the DWI protocol were used (TR = 325 ms; TE1 = 4.30 ms; ΔTE = 4.76 ms).

DWI data of the independent database were acquired on a 1.5 Tesla Sonata scanner (Siemens, Erlangen, Germany) with similar sequence parameters at slightly lower slice thickness (72 slices; resolution 2×2×2 mm^3). Three sets of DWI data were recorded for subsequent averaging to improve the signal-to-noise ratio (total scan time 45 minutes).

2.5. Behavioral data acquisition

We acquired fMRI time-series and T1-weighted anatomical images in one session, whole brain DWI-data and explicit behavioral post-hoc ratings in a second scanning session within two weeks**.** To assess the impact of high post-hoc rating accuracy on age change-related activations at the second level (see **Results**, **Figure 3.4**), age-rating

performance (see **Results**, **Table 3.2**) was used to discriminate most accurate (n = 5) from average (n = 14) age-raters. Based on the actual distribution of rating errors accumulated over all stills, the lower quintile of below-average raters (P20, n = 5) was excluded (see **Results**, **Table 3.2**).

2.6. Preprocessing and first level statistical analysis

All MRI data were processed using FSL [**71**] and FreeSurfer [**72**]. First-level fMRI and DWI data were unwarped (using *PRELUDE* / *FUGUE*), motion- and eddy current-corrected (using *MCFLIRT* [**73**] and *eddy_correct*, respectively), and brain-extracted (using *BET* [**74**]; all part of FSL). First-level fMRI analysis was carried out by applying the General Linear Model (GLM) within *FEAT* using *FILM* [**75**] prewhitening, with motion outliers (detected by *fsl_motion_outliers*) being added as nuisance regressors. GLM is based on the use of convolution models [**76**] which assume a linear time-invariant system that has been introduced to allow forward modeling of the BOLD response enabling to detect areas of brain activity in fMRI.

High-pass temporal filtering of the data and the model was set to 100 seconds based on the power spectra of the design matrices (estimated by *cutoffcalc*; all part of FSL). Regressors were included as explanatory variables in *FEAT*'s three-column format defining onset, duration and strength of the stimuli. Parametric intensity modulation of graded stimulus strength for the different explanatory variables is described below. To capture slight deviations from the model, temporal derivatives of all explanatory variables convolved with *FEAT*'s gamma hemodynamic response function (HRF) were included.

2.7. Surface based registration and higher level analysis

In order to take advantage of surface-based registrations and statistical analyses, FreeSurfer was used for segmentation and surface reconstructions of the structural T1-weighted MRIs. Employing boundary-based registration (*bbregister* [**77**], part of FreeSurfer), robust and accurate within-subject cross-modal alignment of functional and anatomical space was achieved and used for intra- and surface-based spherical averaging in the final inter-subject registration of anatomical, fMRI and DWI space. Concatenating the functional-to-anatomical transformation of each subject with the surface-based registration to FreeSurfer's spherical average [**78**], *FEAT*'s first-level contrast-of-parameter estimates (COPEs) and their variances (VARCOPEs) were resampled to the common *fsaverage* surface. Surface-based spatial smoothing of 5 mm FWHM was applied. At the group-level, a mixed-effects (ME) GLM analysis [**79**] was performed (using *mri_glmfit*, part of FreeSurfer) identifying vertices in which brain (de-)activation was correlated with, age, gender and global optical flow processing.

At the second level, thresholding was performed by non-parametric permutation-based cluster mass inference [**80-84**] and included within-contrast correction for multiple comparisons across all vertices of the *fsaverage* surface. Across the contrasts tested, Bonferroni's correction was applied. Interactions between the explanatory variables of interest (gender and age change, global optical flow) were modeled at the first and assessed at the second level. The volunteers' gender was explicitly modeled at the second level to test for between-gender differences. Only results with family-wise error rate (FWER) corrected p-values < 0.05 are reported, coordinates are given in MNI305 space.

2.8. Modeling changes of age, gender and optical flow

Since face stimuli underwent continuous temporal changes during morphing, all explanatory variables were modeled according to their change over time. For age and gender (see **Figure 2.5**), this was achieved by time-binning at the video frame rate (24 fps). Effectively, this comes close to binning at infinitesimal small steps which is equivalent to the first derivative of the stimulus-over-time function itself (see below). Scaling of each regressor was set to a relative maximum of 1. In order to determine accurate stimulus response functions, especially for age and gender, we extensively evaluated our paradigm and the stimuli employed by various post-hoc ratings performed between seven days and two weeks after the functional runs. Thereby, we empirically identified unbiased stimulus response functions for age and gender, later used for modeling in the fMRI analysis (see below).

2.8.1. Modeling Age

First, we instructed our volunteers to rate their subjective impression of how much facial age actually changed across morph sequences spanning an age spectrum similar to the original paradigm (**Figure 2.3A**). To minimize potential rating biases, the (n = 121) face stimuli were morphed to another average-aged male face of 33 years not contained in the original set. I.e., the subjects were familiar with the faces (except for the averaged-age male) but not with the particular morphs displayed. Single start-to-target morphs were randomly played forwards or backwards for the rating. In a second experiment, the task was to estimate the age of (n = 201) face stills in years (see **Figure 2.3B**).

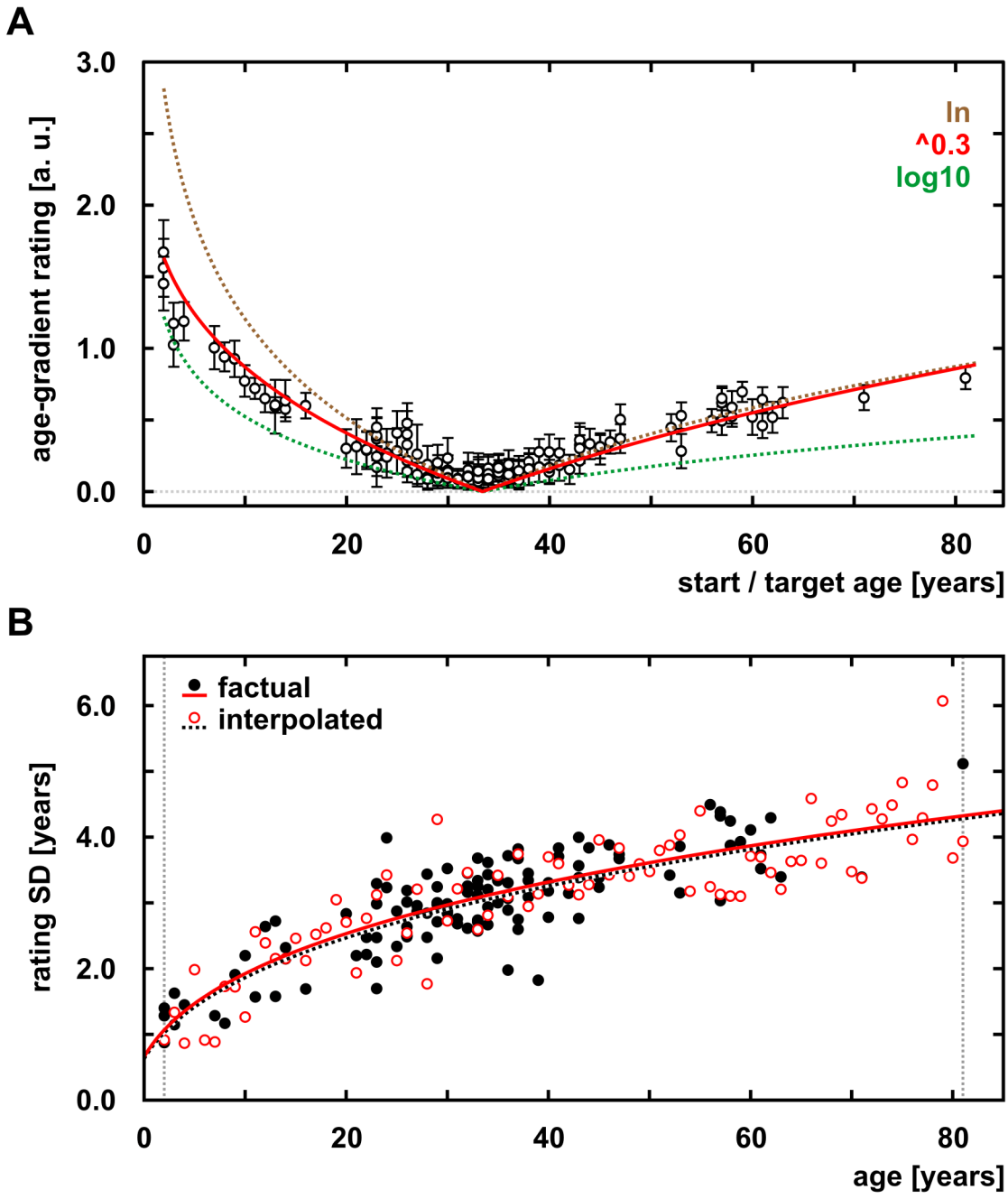

Figure 2.3: Psychometrics of facial age changes

(**A**) Subjective facial age-gradient assessment (rated on a 6-point visual analogue scale, maximum scaled to 3.0 arbitrary units [a.u.]) followed Stevens' (^0.3) better than Weber-Fechner's law (log10) or a natural logarithmic transformation (ln). All face stimuli (n = 121) were morphed to an average-aged male face of 33 years, the morphing sequence was randomly played forwards or backwards for the rating (circles with error bars; n = 24 subjects). (**B**) Facial aging (x-axis; objective age in [years]) increased the variability of subjective age ratings (y-axis; SD, standard deviation of estimated age in

[years] across n = 24 subjects). Rating accuracy of factual (n = 121 stimuli of real faces) and interpolated age (n = 80 intermediate face stimuli from the morphing algorithm; one randomly selected for each annual increment between 2 and 81 years of age) did not differ significantly (p = 0.97).

For this purpose, stills of all (n = 121) real faces and of (n = 80) interpolated age models were displayed randomly. In both of these stimulus samples, real and interpolated age models, facial aging increased subjective age rating variability across our (n = 24) subjects similar to the group-ratings of young and old faces reported by Ebner [**85**]. No significant difference between real and interpolated faces was detected and exponential fitting revealed congruent curves.

On a 6-point visual analogue scale, subjective age-gradient ratings for the (n = 121) separate face morphs (**Figure 2.3A**) were best encoded according to Stevens' law of psychophysics [**86**], a refinement of Weber-Fechner's law which, according to Ziehen [**87**], had already been proposed by Plateau in 1873:

$$\psi\left(I\right) = k \times I^{a} \qquad (\boldsymbol{E1})$$

where ψ(I) is the psychophysical stimulus response function relating the subjective magnitude of sensations / perceptions to the evoking stimulus (I), k is a proportionality constant and a is a variable exponent that depends on the actual type of sensory stimulation. Here, the subjective magnitude of age gradients spanned by morphing was related to the difference between start and target age, both transformed by a power exponent of 0.3 (see **Figure 2.3A**). According to these data, psychophysical age processing is approximately described by:

$$y(x) = k \times x^{0.3} \qquad (\boldsymbol{E2})$$

where x corresponds to objective absolute age (at k = 1). Since age change refers to the difference between two time-points, the function for discrete time-binnings becomes equal to:

$$y(t_{a \to b}) = \left| x_b^{0.3} - x_a^{0.3} \right| \qquad (\boldsymbol{E3})$$

where a / b set the time interval ($t_{a \to b}$; e.g., from the beginning of the morph to its end, when the target face is reached) and $x_{a/b}$ are the corresponding age values (e.g., start and target age; range [2 to 81 years]). Given that age changed continuously with every frame of the morphing video, with interpolated frames being as realistic as the true endpoints (see also **Figure 2.3B**), $x_{a<i<b}$ is exactly determined by the time elapsed. For infinitesimal small bins, psychophysical age change then corresponds to the first derivative of (***E2***):

$$f'(x_a) = y(t) = \left| -\frac{3}{10} \times \frac{1}{x_i^{7/10}} \right| \qquad (\boldsymbol{E4})$$

where x_i is the actual encoded age which changes from frame to frame during the morphing sequence. Given that it remains unclear to what extent facial age estimates are based on local feature, internal configuration, texture and global shape processing [**42, 88-90**], this was considered the optimal approach to implement and model continuous changes of facial age. Deviation from linear transition values reflects the fact that subjective facial aging is relatively up-weighted during initial morphing periods and younger absolute ages (see **Figure 2.5A**). Applied to age changes within individuals, for which only limited data of unstandardized and scarcely suitable images

are available [**42**], this would reflect a modeling bias towards the earlier development of face shape that prevails over textural changes such as wrinkle formation during later aging [**42**] or their disappearance upon cosmetic rejuvenation. Across individuals and their shape differences, however, configural was not forced into any overt advantage over featural processing (see also the flow magnitude lines in **Figure 2.7A**) which can be considered another advantage of our paradigm.

2.8.2. Modeling gender

To investigate the psychophysical processing of gender, especially at intermediate ambiguous stages, (n = 119) sample faces along temporal morph continua across gender (n = 60 morphing sequences) were rated by the volunteers on a 6-point visual analogue scale according to their subjective impression of facial gender or androgyny levels (**Figure 2.4**).

In accordance with previous reports [**28**], subjective gender levels were augmented above linear transition values reflecting the tendency to apperceptive categorization. Gender-level ratings of the faces followed Stevens' power law just as age but were best fitted by a power exponent of 3 along the temporal morph continuum (see **Figure 2.4**), which is also in good agreement with recent data [**28**].

In accordance with the face gender ratings (see **Figure 2.4**), psychophysical gender processing is approximately described by:

$$y(x) = k \times x^3 \qquad (\boldsymbol{E5})$$

where x corresponds to the objective absolute androgyny level (at k = 1).

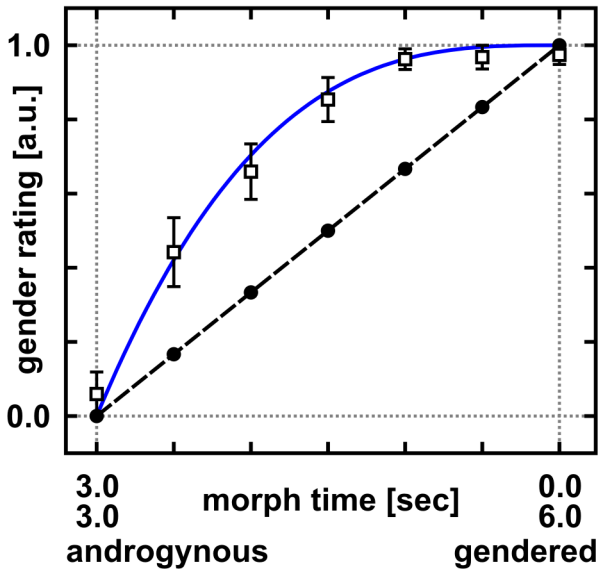

Figure 2.4: Psychometrics of facial gender changes

Face gender ratings (on a 6-point visual analogue scale, maximum scaled to 1.0 arbitrary units [a.u.]) along temporal morph continua (n = 60) across faces of clearly different sex. Subjective ratings by (n = 24) subjects (boxes with error bars, blue line) are augmented above linear transition values (dashed line with black dots), reflecting the tendency to apperceptive gender categorization.

Perceived gender change while morphing a clearly gendered face towards mid-androgyny then simply depends on the difference of androgyny levels between time-points, so the function for discrete time-binnings equals:

$$y(t_{a\rightarrow b}) = \left| x_b^3 - x_a^3 \right| \quad (\boldsymbol{E6})$$

where a / b set the time interval ($t_{a\rightarrow b}$; e.g., from the beginning of the morph to no more than the point when maximum androgyny is reached) and $x_{a/b}$ are corresponding gender levels ([0 to 1]).

Again, these changed with every frame of the morphing video and are exactly determined by the time (t) elapsed. For infinitesimal small bins, gender change is then described by:

$$f'(x_a) = y(t) = \left| -3 \times x^2 \right| \qquad (\boldsymbol{E7})$$

where x is the actual encoded gender value of the face, which changes from frame to frame during the morphing sequence, so that the unsigned first derivative of (***E5***) was used to encode facial gender change (**Figure 2.5B**). Contrary to previous modeling [**28**], peak androgyny was defined as the effective stimulus-of-interest because the cognition of face gender transitions is particularly emphasized at the center of the morph (see **Figures 2.2** and **2.5B**). Slight deviations from the center peak were captured by including the temporal derivative. Since prepuberal faces generally appear less gendered, the androgyny peak of a given morphing sequence tends to be shifted to very young faces. Modeling a temporal derivative accounted for this effect and avoided a secondary bias in testing age-by-gender interactions.

Actual time-binning of both regressors, age and gender, was matched to the frame rate of 24 frames per second (fps), aliasing the stimulus-response function only slightly, with no relevant impact on the subsequent fMRI analysis. Notably, gender change of our unambiguous faces was identically encoded for all morph episodes including gender transitions (n = 60) whereas age change (see above, section **2.8.1.**) obviously depended on the absolute age difference over the morph episode: Since morph duration was kept constant (6 secs), the slope of age changes over time according to (***E4***) was modulated by the age difference between the first and last face of the morph whereas the slope of gender change according to (***E7***) was identical across the morphs containing gender transitions.

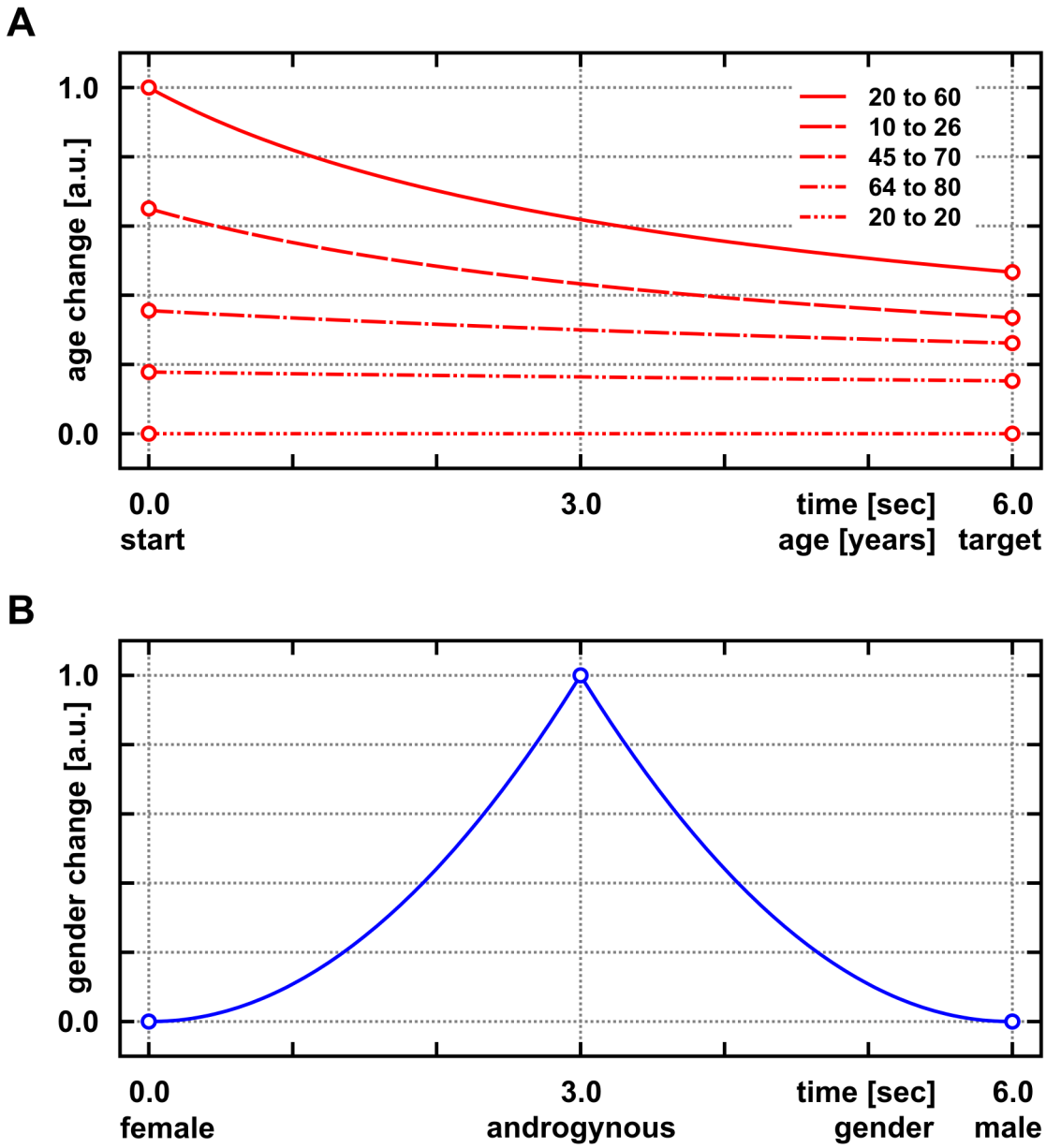

Figure 2.5: Modeling changes of age and gender during face morphing.

(**A**) Differential age change encoded according to Stevens' law of psychophysics (using a power exponent of 0.3; see **Figure 2.3A**). Note that relative facial aging was up-weighted to initial periods of the example morph (see **Figure 2.2**; here: solid red line) and, for identical age differences, to younger absolute ages, i.e. aging from 10 to 26 was assumed to provide a stronger stimulus with more visual cues than aging from 64 to 80 years (dashed vs. double-dotted/dashed line). (**B**) Differential gender change expressed by the first derivative of the function plotted in **Figure 2.4**. Note that peak androgyny was defined as the effective stimulus-of-interest, i.e. the transition of facial gender was emphasized at the center of the morph (see **Figure 2.2** and **Appendix**).

Both models, age as well as gender, were time-binned at the video frame rate (24 fps) and scaled to maxima of 1.0 arbitrary units [a.u.] (see also **Figure 2.5**).

2.8.3. Modeling optical flow

Optical flow [**91**] across time, representing the total amount of motion between successive key frames of the paradigm, was separately modeled to reduce the amount of unexplained variance which would confound the analysis if all morphing transitions were treated the same. On top of age and gender, optical flow during morphing differs between different pairs of start and target faces. Due to the complex concomitant factors determining the shape of the faces as well as the high-contrast edges that result from individually cropping neck, ears and the top of the head, it is impossible to mathematically estimate motion /optical flow prior to rendering. Therefore, the full set of visual stimuli containing the (n = 120) continuous morph sequences displayed in the fMRI paradigm was fed into a customized Simulink [**92**] model estimating optical flow between successive video frames by a Horn-Schunck [**93**] algorithm using MATLAB's video and image processing blockset (**Figures 2.6**, **2.7A**). Optical flow (F) was estimated by the Horn-Schunck method with 30 iterations per key frame pair according to:

$$F = \iint \left[\left(I_x u + I_y v + I_t \right)^2 + \alpha^2 \left(\left| \nabla u \right|^2 + \left| \nabla v \right|^2 \right) \right] dxdy \qquad (\boldsymbol{E8})$$

where Ix, Iy and It are the derivatives of the image intensity values along the x-, y- and time-dimension, respectively, α is a regularization constant and $\left|\nabla u\right|^2, \left|\nabla v\right|^2$ are components of the optical flow vector. First, a vector field representing the inter-key frame motion was estimated, illustrated by flow magnitude lines (**Figure 2.7A**).

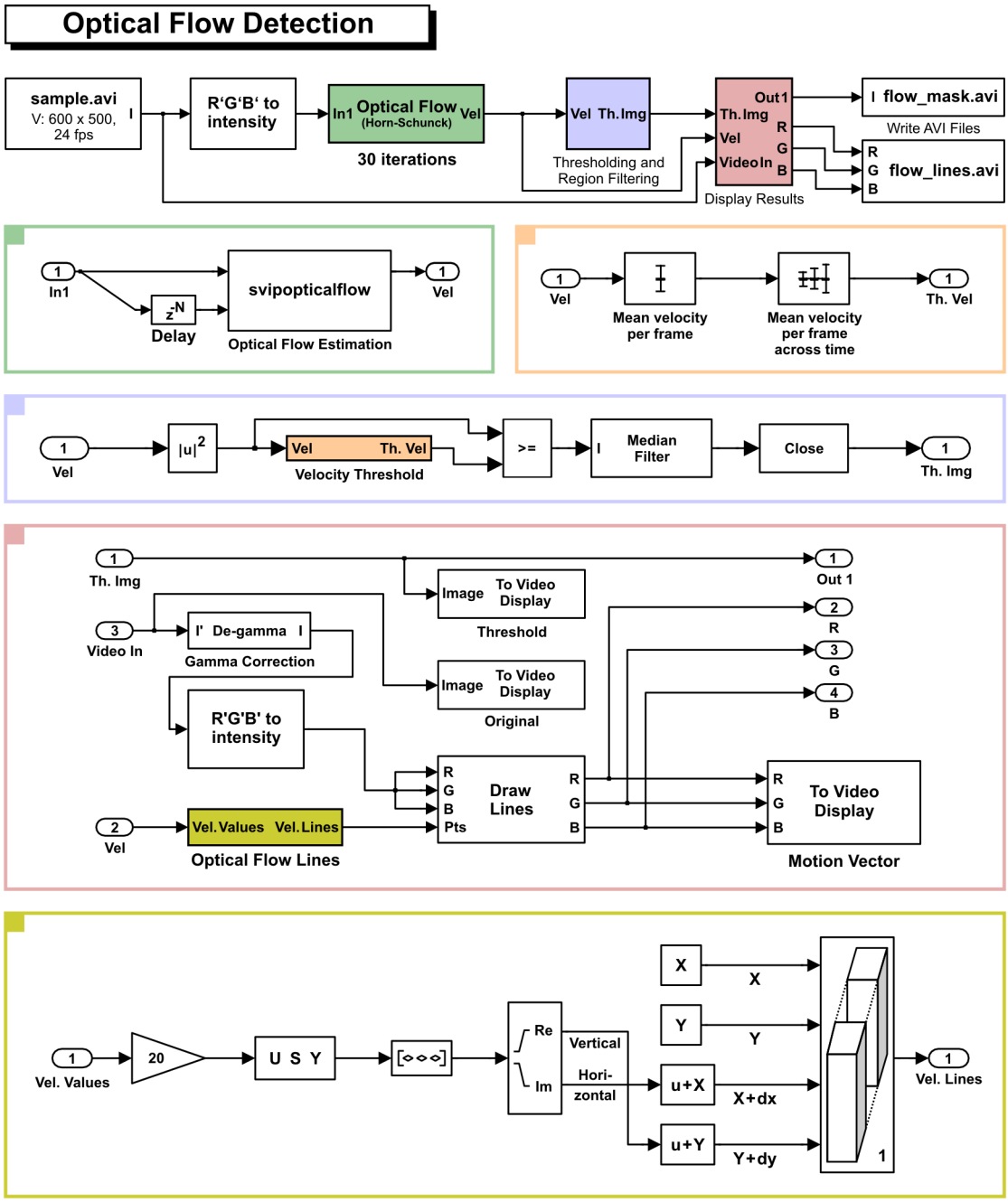

Figure 2.6: Optical flow detection flowchart

Matlab's Simulink model of digital image processing applied to extract motion / optical flow between successive video frames. Speed and direction of motion (see line magnitude images of flow velocities in **Figure 2.7A**) were estimated for the morph sequences using the Horn-Schunck method with 30 iterations per frame pair.

Then, the vector field was converted to a binary mask (see 3rd row in **Figure 2.7A**).

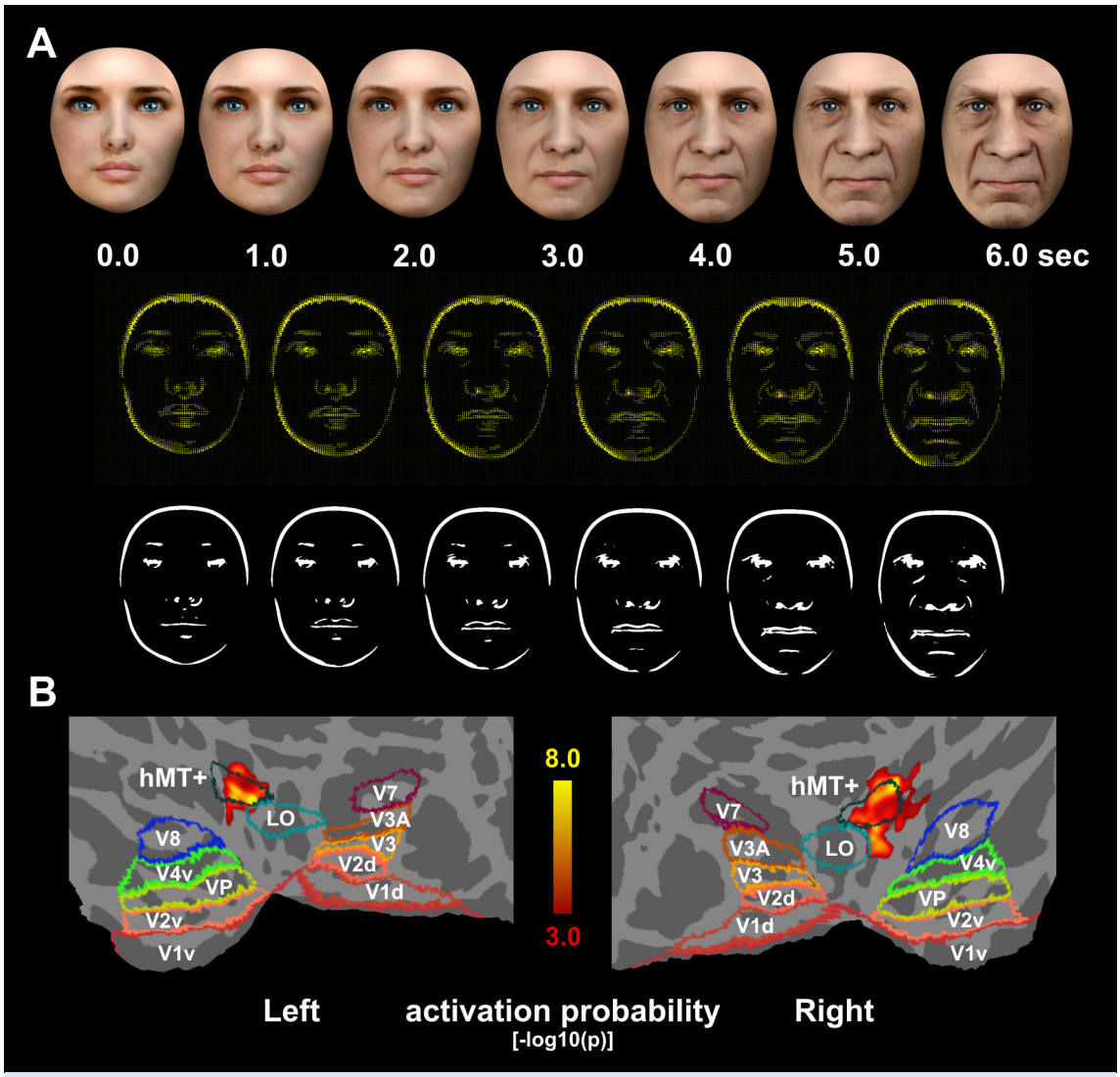

Figure 2.7: Motion / optical flow and associated functional (hMT+) activations

(**A**) Exemplary face morph (top row, also see **Appendix**), line magnitude (2nd row; zoom to enlarge if possible) and binary mask (3rd row) images of optical flow velocities computed by a Horn-Schunck algorithm (see **Figure 2.6**). Overall motion / optical flow was quantified as a surrogate parameter by the sum of flow magnitudes within the corresponding mask between successive key frames. (**B**) Motion-/flow-related activation derived from the group-level analyses (n = 24 subjects, FWER-corrected $p < 0.05$, [-log10(p)] color bar) on posterior cortical flat maps of both hemispheres. Additionally, ventral (v) and dorsal (d) visuotopic labels (V1-8, Vp, LO, hMT+) of the SuMS [**94**] database, transformed from Caret's PALS atlas [**95**] into FreeSurfer's average surface space, are displayed. To generate flat maps without curvatures the surfaces were cut open along the same anatomical markers on both hemispheres.

The sum of unsigned flow values within that mask M described the total amount of motion between successive key frames of the paradigm and was robustly estimated as a surrogate parameter of global flow intensity R at one-second intervals according to:

$$R = \sum_{y=1}^{n}\left(\sum_{x=1}^{n} M^{x,y}\right) \qquad (\boldsymbol{E9})$$

Given that all pixels exhibiting optical flow could not be entered as separate explanatory variables to preserve sufficient degrees-of-freedom for the analysis, and considering that the expansions and contractions involved in our face morphing were quite smooth, i.e. cross-correlated, it seemed both practical and sensible to integrate global optical flow as a confound regressor into our paradigm. Note that optical flow detection on a frame-by-frame basis becomes less robust, i.e. time-binning above 1 fps does not improve the results.

Functional activations associated with global optical flow are shown on bilateral flat maps with additional visuotopic labels [**96-100**] of the SuMS [**94, 95, 101**] database, http://sumsdb.wustl.edu/, to facilitate orientation and to illustrate the spatial correspondence of our clusters with the hMT+ atlas labels (see **Figure 2.7B**).

2.9. Quantifying relative response magnitudes

Relative response magnitudes were quantified based on mean within-cluster contrast-of-parameter estimates (COPEs) normalized to the respective minimum (in **Results; Figures 3.2** and **3.4B**). Scaled to the peak-to-peak height of the effective regressor and divided by the mean-over-time of the preprocessed (i.e. filtered) EPI

time-series from lower-level GLM analyses, mean COPE values are equivalent to mean percentage BOLD signal changes. Given the constant scaling for a particular contrast fitted, normalized COPEs translate directly into estimated ratios of the associated signal changes within (**Figures 3.2** and **3.4B**) but not across contrasts. First-level COPEs from each cluster of the 12 participating males and females were tested for hemisphere and gender effects (n = 24; ANOVA, factorial within-/across-subjects design). In order to obtain interpolated model fits for illustration at individual peak activations within the age-responsive clusters, age-gradients were trichotomized into equal intervals according to formula (***E3***) (see before) in a separate first-level analysis. Here, average signal changes over time were reconstructed according to the GLM using the temporal mean of the filtered time-series, the basis functions and their corresponding parameter estimates (see **Results** and **Figure 3.3**).

2.10. Probabilistic tracking and modeling

DWI data were processed using *FMRIB's Diffusion Toolbox* (*FDT*, part of FSL 4.1). Up to two fiber orientations were modeled and the corresponding probabilistic distributions of diffusion parameters were built up at each voxel (using *bedpostx*, part of *FDT*). Probabilistic tracking and modeling multiple fiber orientations [**102**] was essential because of the high number of crossing fibers in the areas under examination. Subsequently, probabilistic tractography was performed by *probtrackx* (part of *FDT*) on the same (n = 24) subjects from which the functional data were recorded, as well as on the independent database of (n = 46) different subjects included for validation, to investigate the structural connectivity between the cortical regions related to either

age or gender processing at the individual gray / white matter boundary surface. After transforming functional clusters obtained at the second level back to individual surface space of the anatomical scans, each cluster mask was defined as a seed with all the others serving as potential targets. A total of 10^4 samples was sent out from each tracking point. Stop and waypoint masking was used to exclude indirect routes. Upon slight spatial smoothing (2 mm FWHM), probabilistic seed-to-target connectivities were then averaged on FreeSurfer's common *fsaverage* surface (see **Figure 2.3**). Probabilistic pathways were transformed to, added and thresholded in MNI space for visualization (using FSL's nonlinear 1 mm MNI template as target space; see 3D-tract volume rendering, thresholded at ≥ 100 connecting samples passing through each voxel, displayed on sagittal [x = -36 mm] and coronal [y = -54 mm] projection view planes in **Results**, **Figure 3.5**).

2.11. Cross-correlations and minimum intersection maps

Minimum intersection maps and vertex-wise spatial cross-correlations between fMRI activation probability values and tractography-based connectivity scores were calculated to assess spatial correspondence between functional activation and structural connectivity patterns (**Figures 2.8**, **3.6** and **3.7**). Thereby, we tested for similarities between the spatial distribution of activation probabilities on the one hand and connection probabilities on the other. The rationale behind this analysis was that if the spatial profile of a connection between A and B predicts the activation profile in A, then this suggests that the connection between A and B is involved in the brain processes required to produce the activation in A. We analyzed the similarities

between these structural and functional profiles using two approaches: First, we calculated minimum intersection maps (see **Figure 2.8** for further explanation) between functional activation probability and structural connection probability maps. Minimum intersections, both spatial and histogram-based [**103**], are established methods to assess image similarities.

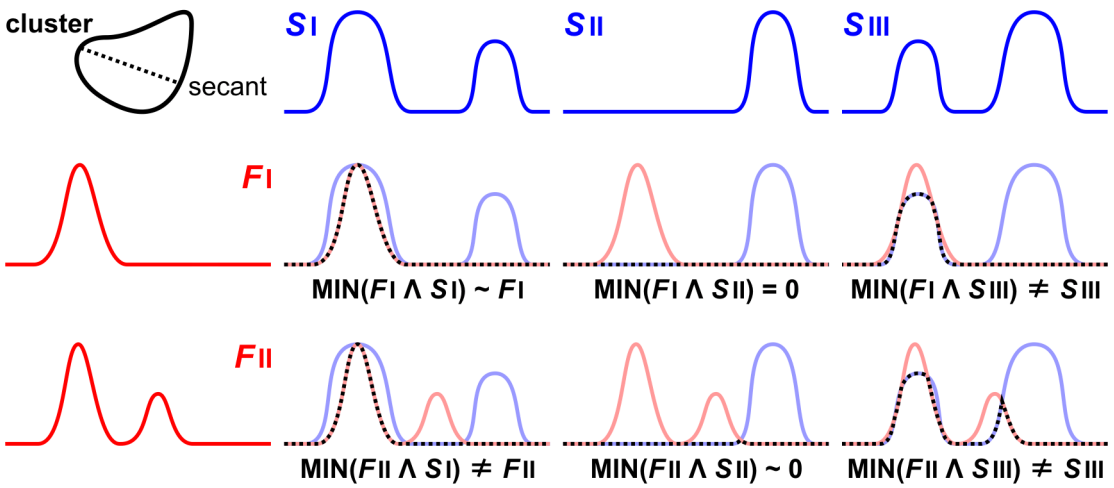

Figure 2.8: Schematic illustration of minimum intersection maps

Minimum intersection maps are generated between different profiles of functional activation (red) and structural connectivity (blue). The profiles are normalized, i.e. scaled to the same min/max range. To build the minimum intersection (dotted), the minimum (MIN) of the two is considered at each point along the profile. Minimum intersection peaks indicate different degrees of spatial correspondence between high structural connectivity (*S*) and functional probability (*F*) values: Minimum intersection maps resembling *F* signify concordant presence of *F*- and *S*-peaks (left and upper right minimum intersects). Note that when *F* and *S* are too dissimilar, the minimum intersection is flat (middle). A non-flat minimum intersect with a sharp peak and displaced compared to *F* indicates a close but out-of-center overlap of *F*- and *S*-peaks (bottom right).

The idea behind using minimum intersection maps in this context was that peaks in the structural connectivity profile should predict peaks in the functional activation profile, but not vice versa, since parts of the structural connections do not necessarily have to

be involved in the task. Minimum intersection maps are appropriate for this kind of analysis, as depicted in **Figure 2.8**. To generate vertex-wise minimum intersection maps (see **Figure 3.6**), the distributions of activation probabilities and average connectivity scores were shifted to zero minima and normalized to their robust maximum values (i.e. the 95^{th} percentile).

Second, we calculated vertex-wise spatial cross-correlations between functional and structural profiles. Cross-correlations were estimated non-parametrically using Spearman's rank correlation coefficient (ρ), all p-values were Bonferroni-corrected for the total number of tests performed (see **Figure 3.7**). Since lower false-positive activation error probabilities reflect higher activation likelihoods, absolute log(p)-values were used for correlation. Insignificant and unidirectional correlations (dotted lines in **Figure 3.7**), i.e. associations of activation probability and connectivity from one cluster to the other but not vice versa, were not considered interpretable.

3. Results

3.1. Functional activations associated with facial age

Functional analysis revealed age change-related activations centered on the posterior inferior temporal sulcus (pITS) lateral to FFG and the posterior angular gyrus area (pANG) of both hemispheres (**Figure 3.1**, **Tables 3.1** and **3.3**). Age change, but not the gender condition, was found to be associated with higher mean left-hemispheric activations ($p = 0.04$, ANOVA; **Figure 3.2**).

3.2. Functional activations associated with facial gender

Gender change-related activations were detected within FFG bilaterally (**Figure 3.1**, **Tables 3.1** and **3.3**), amplifying previous evidence for gender-selective FFG responses [**28, 37**]. Notably, increased face androgyny during across-sex morph transitions activated above the more differentiated gender levels (see **Figure 2.5B** and **Materials and Methods**), and not vice versa as for static stimuli [**28**], illustrating the context dependency of the functional activations. In addition, the right lateral occipitotemporal area (LOT), already implicated by an early PET study [**104**], and the left dorsolateral prefrontal cortex (DLPFC) were involved (**Figure 3.1**, **Tables 3.1**, **3.3**).

3.3. Functional activations associated with global optical flow

Global optical flow was associated with functional activations in the motion-sensitive cortex (hMT+) (see **Figure 2.7B**; **Tables 3.1** and **3.3**), known to respond stronger than

any other area to radial motion, 2D expansions and contractions as well as 3D motion [**105-108**] but which is also important for stereoscopic depth perception [**109**]. In accordance with previous results [**96**], hMT+ activations evoked by attention to all quadrants of the visual field were more extensive on the right hemisphere.

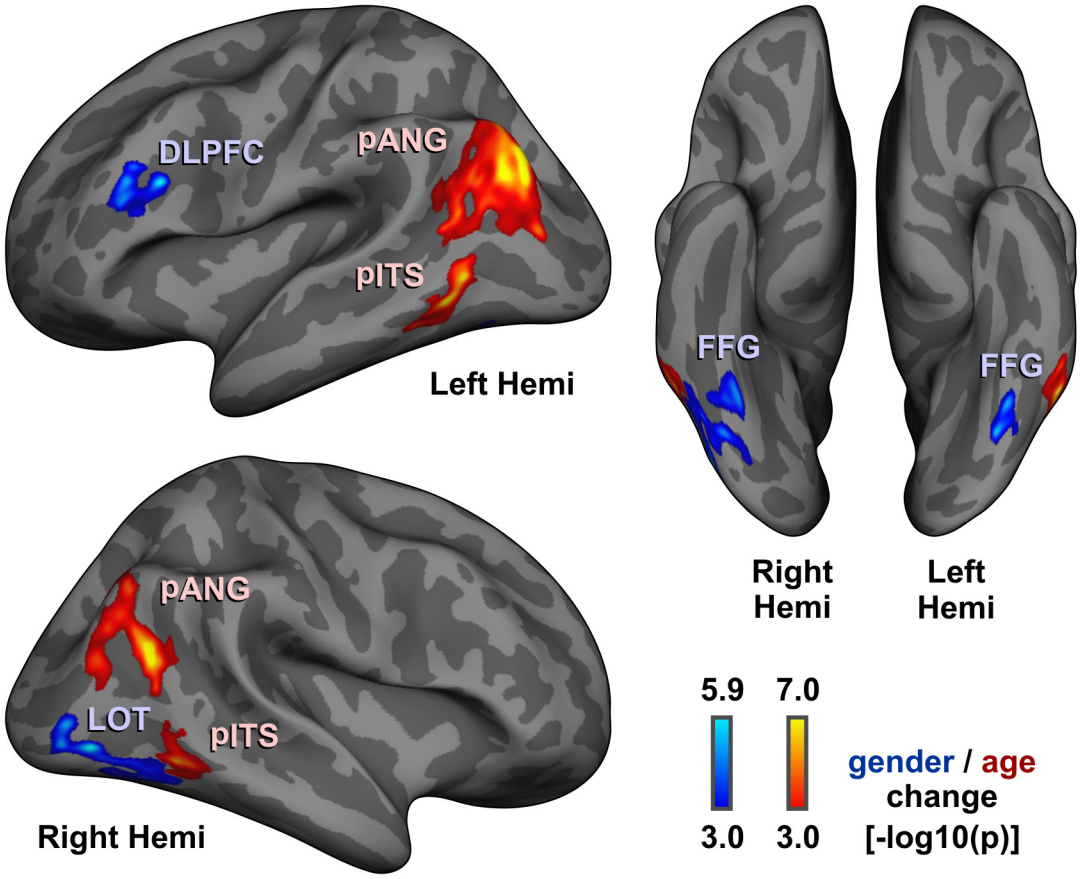

Figure 3.1: Functional activations associated with changes of facial age and gender

Group-level (n = 24) functional activations[1] related to age and gender change, respectively.

[1]Significant activations (FWER-corrected $p < 0.05$) displayed on FreeSurfer's average inflated surface (color bars depict uncorrected activation probabilities [-log10(p)]; also see **Introduction** and **Figures 1.2** and **1.3** about surface reconstruction and inflation of the human brain.)

pANG, posterior angular gyrus area; pITS, posterior inferior temporal sulcus; DLPFC, dorsolateral prefrontal cortex; LOT, lateral occipito-temporal area; FFG, fusiform gyrus

3.4. Group differences and interactions

No significant differences between male and female volunteers and no significant positive or negative interactions between the variables of interest age, gender and optical flow or their relative response magnitudes, i.e. normalized effect size values, were detected. Only age change, as mentioned above, was found to be associated with higher mean left-hemispheric activations (see **Figure 3.2**).

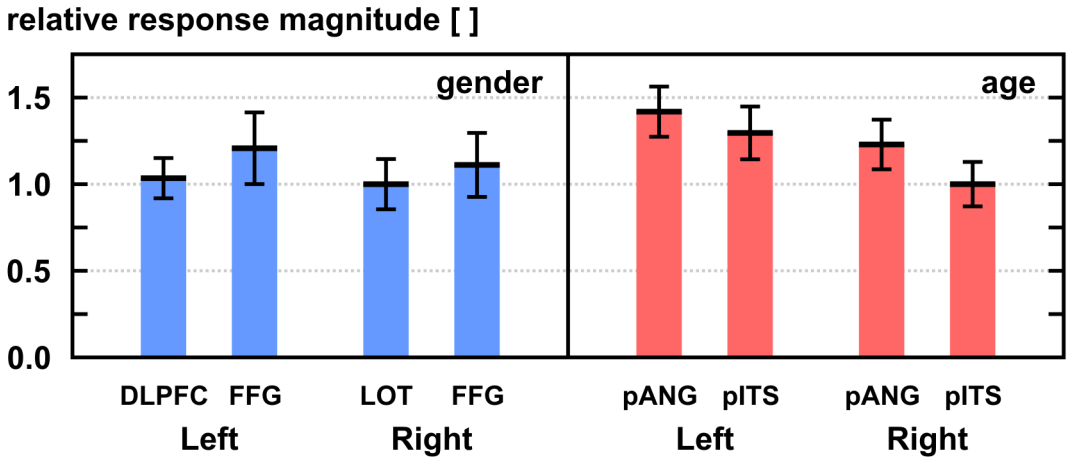

Figure 3.2: Comparison of response magnitudes of functional activations
Quantification and between-cluster/-hemisphere comparisons of effect sizes evoked by facial age and gender changes across (n = 24) subjects. Values of each cluster's mean activation (± error bars) were normalized to the lowest average of corresponding response magnitudes (see also **Figure 3.3**).
pANG, posterior angular gyrus area; pITS, posterior inferior temporal sulcus; DLPFC, dorsolateral prefrontal cortex; LOT, lateral occipito-temporal area; FFG, fusiform gyrus

3.5. Interpolated model fits of individual peak activations

Increasing age-gradients evoked higher signal changes, which were more pronounced for the left than the right hemisphere (also see **Figure 3.2**) and peaked slightly earlier in pITS than pANG ($p \leq 0.05$, ANOVA). Although slightly earlier peaks of pITS activations

compared to pANG may indicate that it is in fact pITS that recruits pANG, full model fits obtained from COPE values are certainly not optimized to detect variable temporal delays in activation onsets or peaks (see **Figure 3.3**).

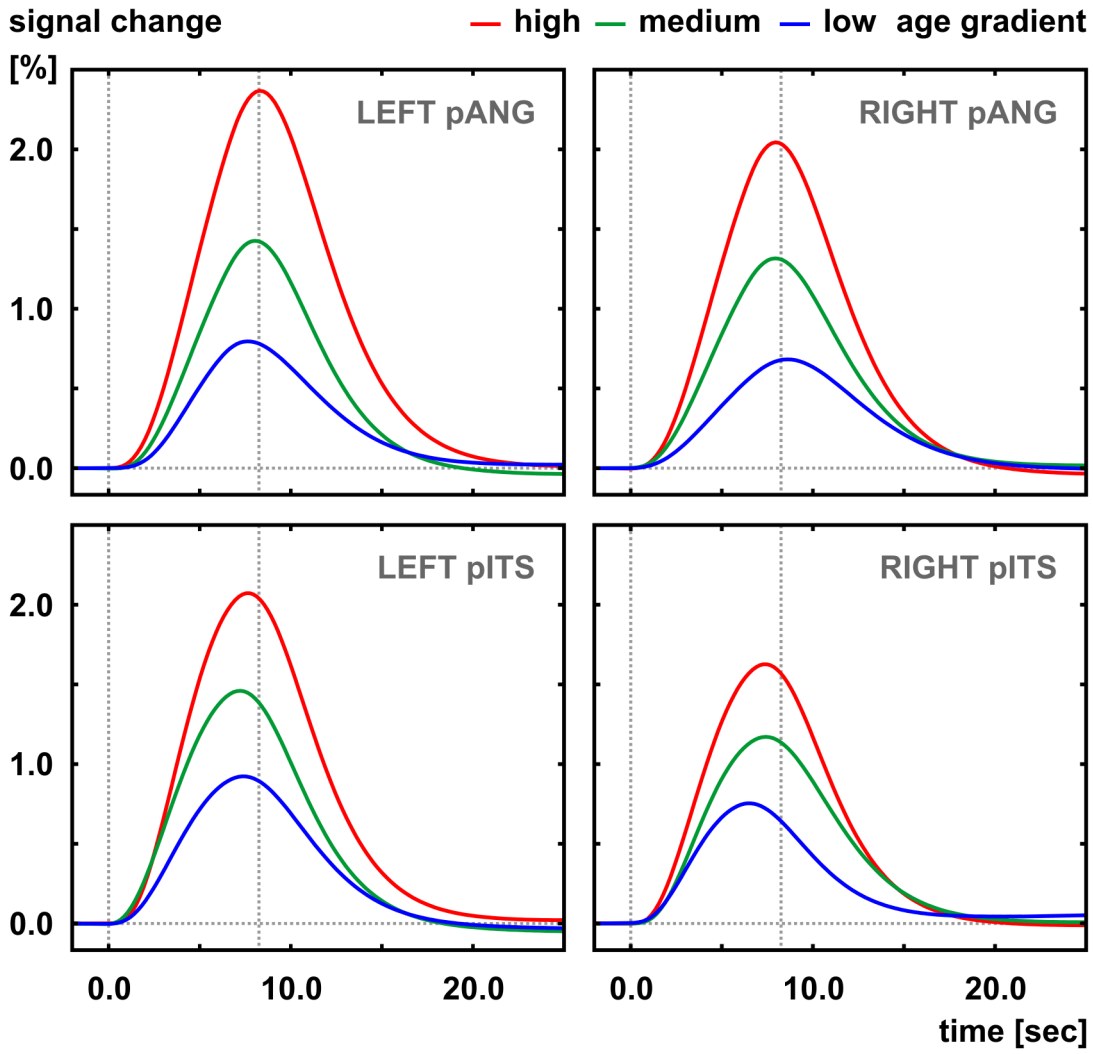

Figure 3.3: Trichotomized intervals of age change

Estimated hemodynamic responses within pITS and pANG in response to low [blue], medium [green] and high [red] age-gradients, reconstructed at individual peak activations within age-responsive clusters using fitted parameter estimates from a separate first-level analysis[1]. Age-gradients were trichotomized into equal intervals according to formula (***E3***); 'low' representing changes from 10 to 20, 'medium' from 10 to 40 and 'high' from 10 to 65 years of age, for example

[1]Signal change ([%]) over peristimulus periods of 25 secs, averaged across (n = 24) subjects. pANG, posterior angular gyrus area; pITS, posterior inferior temporal sulcus

	hemi	cluster	size	Max	CWP	VtxMax
age	left	pANG	2309	8.739	0.0001	142332
		pITS	526	7.307	0.0001	40331
	right	pANG	1177	8.465	0.0001	117820
		pITS	367	6.025	0.0004	5665
rating*	left	pANG*	32	5.045	0.0133	146872
gender	left	DLPFC	370	5.948	0.0005	29235
		FFG	228	5.437	0.0020	92500
	right	LOT	862	5.988	0.0001	35952
		FFG	202	5.107	0.0021	28527
motion	left	hMT+	605	8.816	0.0001	551
	right	hMT+	1204	8.554	0.0001	91197

Table 3.1: Size and probability of significantly activated clusters

Clusters significantly activated by changing facial age, gender and motion / optical flow, respectively (FWER-corrected $p < 0.05$ for $n = 24$ subjects)[1]

[1]hemi, hemisphere; size in [mm^2], CWP, cluster-wise probability (non-parametric cluster mass inference over the entire surface); Max, maximum uncorrected p-value (peak activation probability); VtxMax, vertex of Max on Freesurfer's average surface;

pANG, posterior angular gyrus area (*cluster related to high age-rating competence, see below); pITS, posterior inferior temporal sulcus; DLPFC, dorsolateral prefrontal cortex; LOT, lateral occipitotemporal area; FFG, fusiform gyrus; hMT+, human motion-sensitive MT+ (V5 or MT/MST) area

3.6. Post-hoc age rating performance

Confirmed by own verbal feedback report, their compliance and motivation was limited so that age-rating performance of these subjects at the second session did obviously not correspond to their actual capacities. This was reflected in the disproportionally higher rating errors (see **Table 3.2**) and the more pronounced variability of relative response magnitudes (shown by increased error bars; see

Figure 3.4B) which prompted the exclusion of the lower quintile raters. Considering that implicit age-change processing is rather unlikely to strongly correlate with explicit age-rating accuracy in post-hoc assessments of a limited sample size, a more rigorous attempt of linear modeling the relation between the initial fMRI activations and later rating performance was not conducted.

	age rating error*			
rating	**accumulated**	**averaged[1]**	**quintile**	**group size**
low accuracy	1099 ± 97	9.1 ± 0.8	≤P20	5
average accuracy	856 ± 56	7.1 ± 0.5	>P20/<P80	14
high accuracy	694 ± 58	5.7 ± 0.5	≥P80	5

Table 3.2: Grouped age rating performance
Classification of the subjects into three groups (low, average and high rating accuracy) based on performance distribution. *age rating error in years (± SD), [1]rating error averaged over trials

3.7. Age-responsive areas associated with high age-rating competence

Within left pANG, a cluster above the superior temporal sulcus discriminated the upper quintile (P80, n = 5) of best explicit age raters from average performers (P20-80, n = 14, also see **Table 3.2**) by higher activations (see **Figure 3.4A** as well as **Tables 3.1** and **3.3**).

Here, superior explicit age-rating competence of upper quintile performers enhanced the mean response magnitude in their activation levels associated with facial age more than fourfold relative to average raters (**Figure 3.4B**).

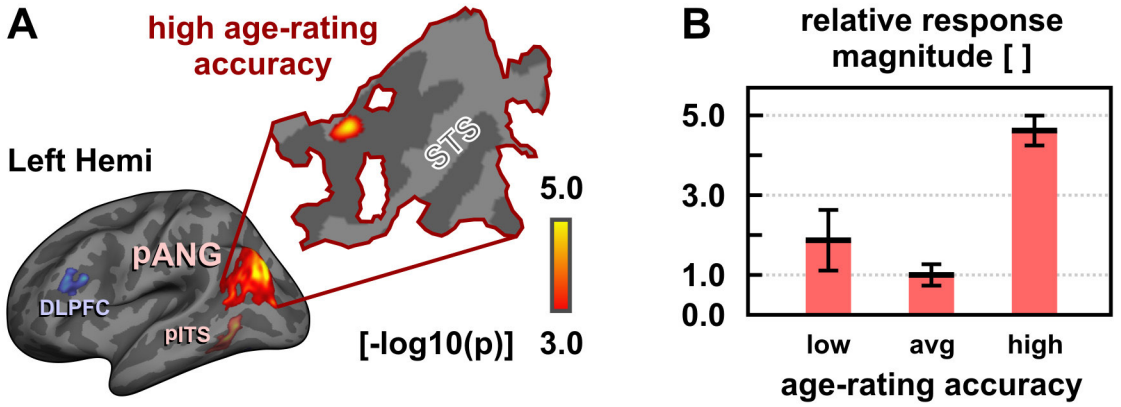

Figure 3.4: Functional activations associated with high age rating competence

(**A**) Increased age-related activation[1] of the most accurate (n = 5) above average age-raters (n = 14). (**B**) Relative to average post-hoc raters (avg, n = 14), high explicit age-rating accuracy (upper quintile P80, n = 5) was accompanied by almost five times the response magnitude ($p < 0.001$) within the left pANG subcluster (see **Figure 3.4A**) during implicit age-change processing.

[1]Significant activations (FWER-corrected $p < 0.05$) displayed on FreeSurfer's average inflated surface (color bars depict uncorrected activation probabilities [-log10(p)]). pANG, posterior angular gyrus area; pITS, posterior inferior temporal sulcus; DLPFC, dorsolateral prefrontal cortex; STS, superior temporal sulcus

3.8. Structural connections between age- and gender-related clusters

For each subject, probabilistic tractography was run between all age and gender change-related clusters on individual brain surface reconstructions. An association tract, the ventral portion of Wernicke's perpendicular fasciculus [**110**], was found to interconnect pANG and pITS (**Figure 3.5**). Its almost vertically running fibers connect the posterior inferior parietal lobule, namely the angular gyrus ('pli courbe'), and the parieto-occipital transition, namely the second parieto-occipital 'pli de passage' of Gratiolet [**111**] or gyrus parietalis inferior posterior [**112**], with the inferior temporal area [**113**].

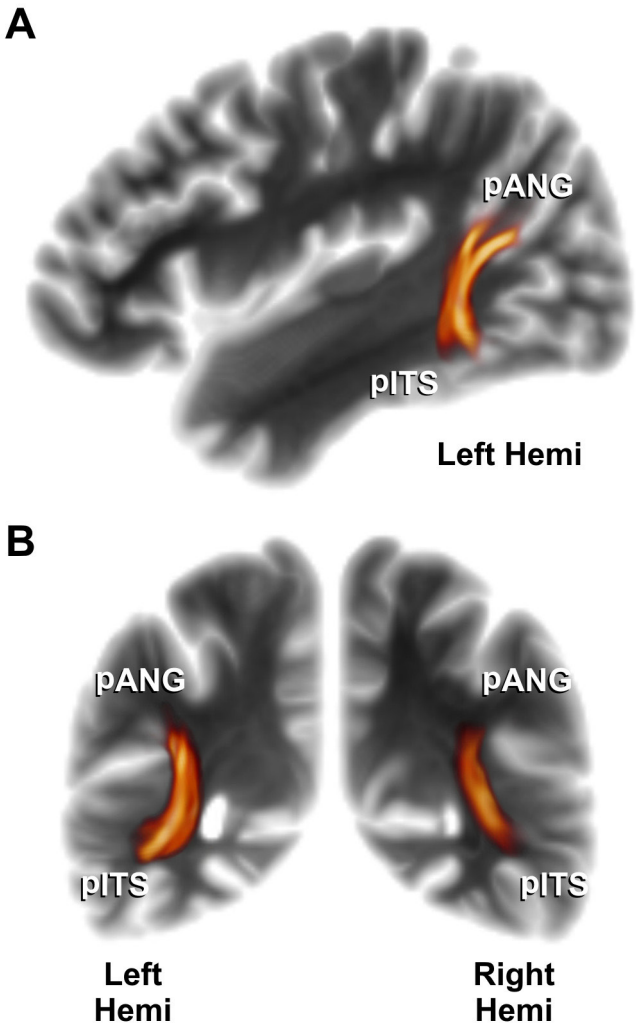

Figure 3.5: Association pathways subserving facial age processing
Ventral portion of Wernicke's perpendicular fasciculus (WpF) connecting pANG and pITS (average probabilistic path distribution connecting the functional clusters of n = 24 subjects, using FSL's nonlinear 1 mm MNI template as target space; thresholded at ≥ 100 connecting samples passing through each voxel, displayed on sagittal [x = -36 mm] and coronal [y = -54 mm] projection view planes; see **Materials and Methods**)
pANG, posterior angular gyrus area; pITS, posterior inferior temporal sulcus

Other cortico-cortical pathways, such as fibers of the superior longitudinal and fronto-occipital fasciculi connecting FFG, pANG and DLPFC (schematically displayed in **Figures 3.8** and **4.1**), are not rendered for display and revealed lower connectivities,

except for some clusters located very close to each other (e.g., FFG and LOT; see **Discussion**, log-transformed connectivity scores in **Figure 3.7**).

Commissure connectivities between clusters related to age or gender processing (n = 32) remained negligible, i.e. less than 0.1 ‰ of the total number of samples sent out from all cluster vertices reached the target.

	hemi	cluster	MNI305 X, Y, Z			vE	BA	annotation
age	left	pANG	-41.0	-74.5	27.0	P*G*	39	inferior parietal
		pITS	-54.1	-55.8	-8.5	P*H*	37	inferior temporal
	right	pANG	46.7	-59.3	19.5	P*G*	39	inferior parietal
		pITS	54.2	-53.5	-9.4	P*H*	37	inferior temporal
rating*	left	pANG*	-42.4	-56.6	25.5	P*G*	39	inferior parietal
gender	left	DLPFC	-36.9	19.5	22.1	F*D*	46	inf. front. sulcus
		FFG	-39.1	-67.9	-17.2	P*H*	37	fusiform
	right	LOT	42.4	-77.3	-5.4	O*A*	19	lateral occipital
		FFG	36.4	-56.0	-16.4	P*H*	37	fusiform
motion	left	hMT+	-42.6	-79.6	0.1	O*A*	19	middle occipital
	right	hMT+	46.7	-58.9	0.4	P*H*O	19	middle temporal

Table 3.3: Location of significantly activated clusters

Clusters significantly activated by changing facial age, gender and motion / optical flow, respectively (FWER-corrected $p < 0.05$ for n = 24 subjects)[1]. Note that although P*H* (area basalis parietalis) largely corresponds to BA 37 (area occipitotemporalis), von Economo considered it to belong to the parietal instead of the temporal lobe [**114**].

[1]hemi, hemisphere; MNI305, coordinates in MNI305 standard space [mm]; vE/BA, von Economo [**114**] / Brodmann [**115**] area; annotation, anatomical labels; pANG, posterior angular gyrus area (*cluster related to high age-rating competence); pITS, posterior inferior temporal sulcus; DLPFC, dorsolateral prefrontal cortex; LOT, lateral occipitotemporal area; FFG, fusiform gyrus; hMT+, human motion-sensitive MT+ (V5 or MT/MST) area

3.9. Linking connectivity and activation patterns

In order to characterize the extent to which different structural seed-to-target connectivities drive activation patterns, we generated minimum intersection maps (**Figure 3.6**, also see **Materials and Methods**, **Figure 2.8**) and examined spatial cross-correlations between surface connectivity scores and activation probabilities (see **Materials and Methods**, **Figure 3.7** as well as **Discussion**).

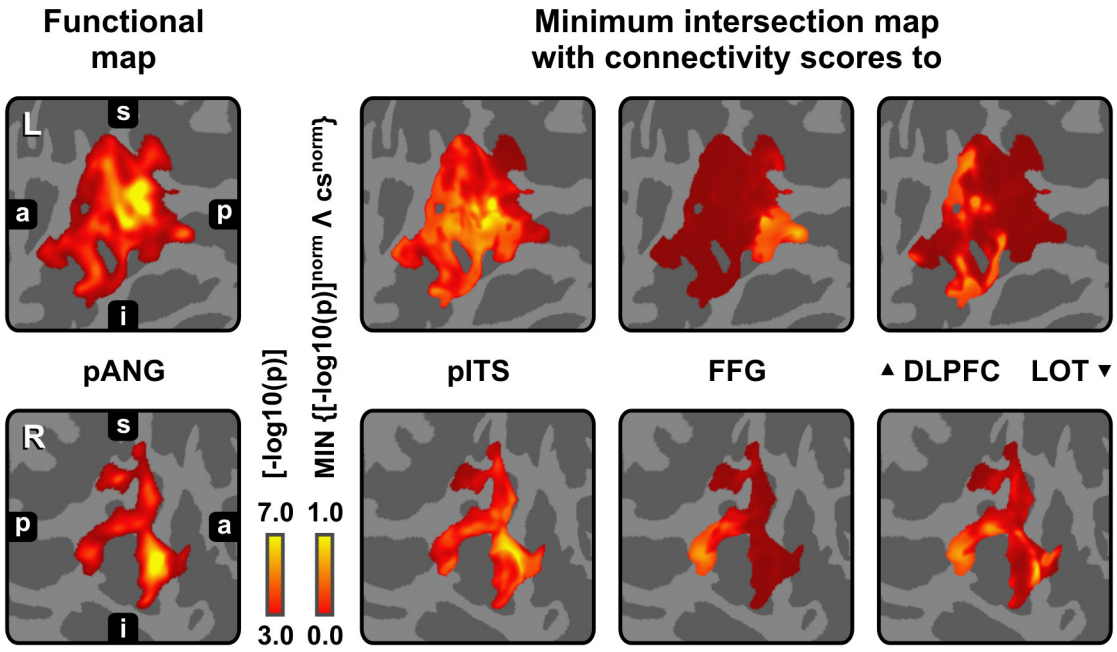

Figure 3.6: Minimum intersection maps of age change related clusters

Activation probabilities (left) and minimum intersection maps (right; illustrating scaled spatial cross-correspondence, see also **Materials and Methods**, **Figure 2.8** for a schematic explanation) with normalized surface connectivity scores [cs] to ipsilateral pITS, FFG, left DLPFC and right LOT clusters (n = 24).

pANG activations are, on average, associated with close intrinsic connectivity to pITS and some posterior connections to FFG (see **Figure 3.7**, for cross-correlation plots of the n = 24 and n = 46 independent subjects).

pANG, posterior angular gyrus area; pITS, posterior inferior temporal sulcus; DLPFC, dorsolateral prefrontal cortex; LOT, lateral occipitotemporal area; FFG, fusiform gyrus; Orientation labels: L, left; R, right; a, anterior; p, posterior; s, superior; i, inferior

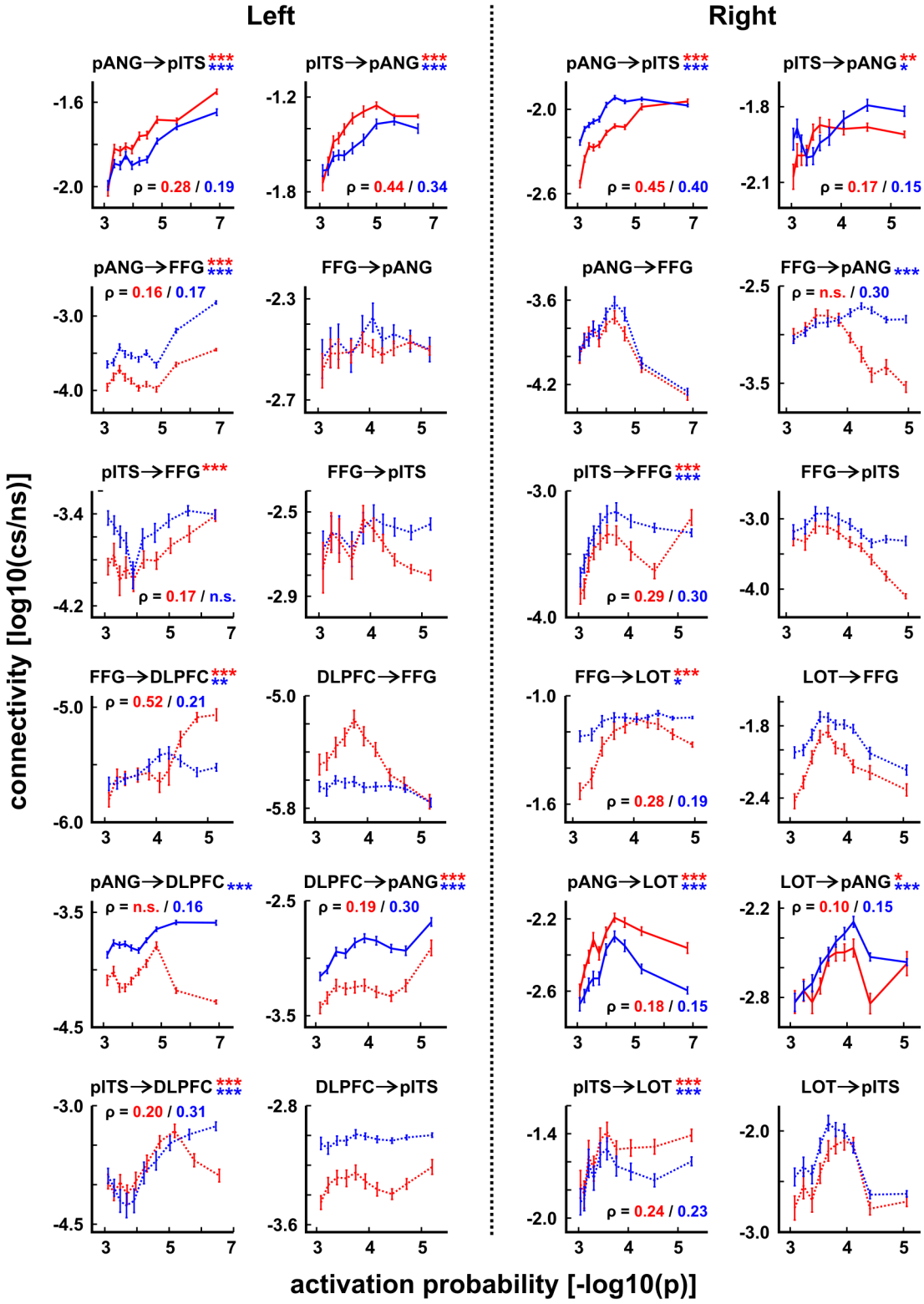

Figure 3.7: Functional and structural spatial cross-correlation plots

Vertex-wise spatial cross-correlation plots (± SEM)[1] between activation probabilities ([-log10(p)]) and structural connectivities ([log10(cs/ns)], with [(cs/ns)] reflecting the ratio of connecting to the number of samples sent out from each vertex) for clusters related to

age and gender change (see **Figure 3.1**), based on two samples: (n = 24) paired with functional data [red] and (n = 46) independent subjects [blue].

[1]SEM, standard error of the mean; */**/***: FWER-corrected p < 0.05/0.01/0.001; n.s., not significant, with Spearman's ρ displayed for the paired / independent sample when significant

pANG, posterior angular gyrus area; pITS, posterior inferior temporal sulcus; DLPFC, dorsolateral prefrontal cortex; LOT, lateral occipitotemporal area; FFG, fusiform gyrus; STS, superior temporal sulcus; orientation labels: L, left; R, right

The minimum intersection maps and the spatial cross-correlation plots (see **Figures 3.6** and **3.7**) are based on the hypothesis that if there is a straight structural connection between a pair of functional regions, where this connection itself is directly involved in the cerebral processing, then the most confident location of high fMRI activation within the regions should be close to the loci of strongest structural connectivity between them, i.e. the patterns of functional activations and anatomical connectivity should be positively correlated. We tested this hypothesis on all clusters responsive to age and gender change.

3.9.1. Minimum intersection maps

Minimum intersection maps revealed that for pANG, lowest type I activation error probabilities were in proximity to high pITS connectivity (**Figure 3.6**), indicating pITS' ability to directly recruit pANG for age processing and vice versa. We show this for the larger age-responsive cluster, pANG, as it is more informative than for the smaller pITS. Dorsal pANG activations demonstrated additional potentially relevant connections to FFG, especially on the left (**Figure 3.6**), but just on this tractography seeding end (i.e. FFG activations were not consistently related to their pANG connectivity; see

Figure 3.7), and pANG's overall connectivity to the FFG cluster remained comparatively low. These connections, which were originally discovered by Wernicke [**116**] based on anatomical examination of monkey brains [**117**], correspond to fibers of Wernicke's perpendicular fasciculus between the angular and fusiform gyri [**118**].

3.9.2. Spatial cross-correlation plots

The by far most consistent spatial cross-correlations between activation probabilities and average connectivity scores were detected for pANG and pITS at the group level (see **Figure 3.7**; results exclusively shown for association tracts). Commissure connectivities were also tested but revealed no significant vertex-wise spatial cross-correlations with corresponding activation probabilities. Note that cross-correlations were most consistent for pANG and pITS (upper row of **Figure 3.7**) but connectivity ratios tend to get bound earlier at maximum values than corresponding activation probabilities. In general, positive correlations were slightly stronger for the sample with paired fMRI and DWI data (n = 24) compared to the independent sample from the DWI database (n = 46). However, the latter largely replicate and confirm generalizability of the results.

3.10. Functional brain network for age processing

The activations elicited by age and gender change, i.e. continuously alternating facial age and androgyny levels, the existing fiber connections between age- and gender-change related clusters and the extent to which the spatial distribution of the highest activation probabilities correlate to the highest structural connectivity enables us to

derive a model (**Figures 3.8** and **4.1** further commented in the **Discussion**) illustrating how the ventral stream, pITS in particular, interacts via Wernicke's perpendicular fasciculus (WpF) with the posterior magnitude-encoding and approximate number system [**119, 120**], pANG in particular, to quantify the varying age of faces.

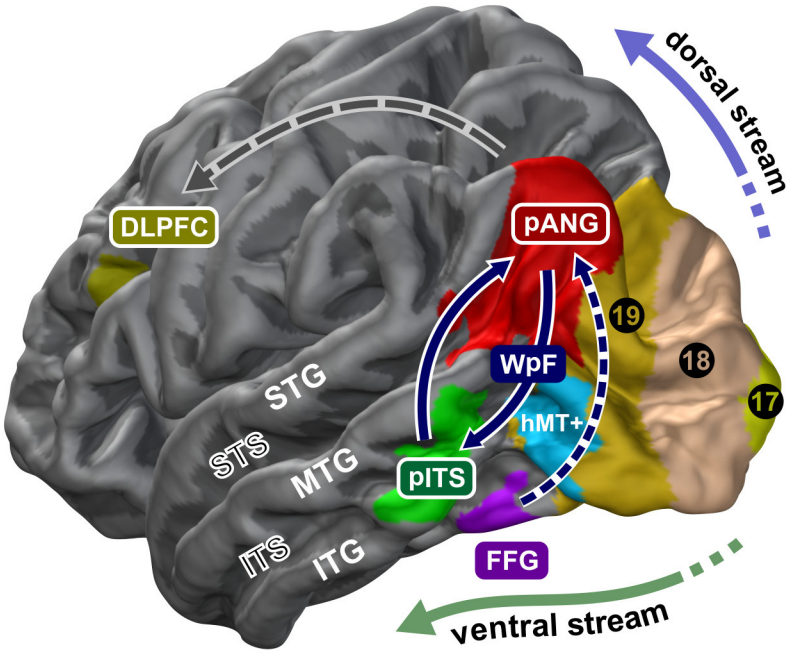

Figure 3.8: 3D model illustrating the age processing network

Left-hemispheric model on the rendered average surface showing functional clusters detected in response to age- (pITS and pANG), gender (FFG and DLPFC) and optical flow (hMT+) and their proposed main interaction of interest in relation to the visual and the dorsal stream.

pANG, posterior angular gyrus area; pITS, posterior inferior temporal sulcus; DLPFC, dorsolateral prefrontal cortex; LOT, lateral occipitotemporal area; FFG, fusiform gyrus; 17-19, Brodmann's areas forming three visual tiers; hMT+, human motion-sensitive temporal cortex; ITG/MTG/STG, inferior/middle/superior temporal gyrus; ITS/STS, inferior/superior temporal sulcus

4. Discussion

4.1. A distinct functional brain network for processing facial age

Our investigation provides the original description of a distinct functional brain network processing the age of faces and its underlying structural connectivity. Although facial age is of high social relevance and has been shown to influence medial prefrontal activations when presumed personality characteristics of individual faces are rated [**121**], the neural basis of facial age processing itself had not yet been identified before. According to our data, its primary cortical components – the areas around the posterior inferior temporal sulcus (pITS) and angular gyrus (pANG) – are separate from those processing categorical gender as a rather fixed face attribute that nonetheless varies across different androgyny levels (**Figures 3.1**, **3.8** and **4.1**). Notably, the age-processing network also expands beyond the proposed face-sensitive core system representing additional changeable aspects and the previously known extended system [**30, 31**] mediating spatially directed attention and imagery [**122**], match decisions based on working memory [**123**], emotional responses [**124**], and even the reward of beauty [**125**] and moral judgments [**126**].

4.2. Linking structure and function

Furthermore, a unique combination of fMRI and diffusion tractography measurements enabled us not only to track anatomical connections between peak activations but to uncover significant vertex-wise spatial cross-correlations between functional BOLD

activations on the one hand and structural connectivity probabilities on the other (**Figures 3.6**, **3.7** as well as **Materials and Methods**, **Figure 2.8**). Such probabilistic association of function and structure substantiates evidence for fiber tracts not just connecting activated areas of interest but being directly involved in transmitting condition-relevant information. In this case, we conclude that age-relevant information is directly transmitted between pITS and pANG by the anterior division of Wernicke's perpendicular fasciculus to which no unambiguous function had been attributed yet. There was no evidence for homo- (e.g. right ↔ left pITS) or heterotopic (e.g. right pANG ↔ left pITS) commissural connections to be involved.

4.3. The ventral visual stream interacts with the angular gyrus

Our results allow us to propose the first coherent model for how the ventral visual stream (vVS) may interact with the angular gyrus area to process different facial ages (**Figures 3.8** and **4.1**). Changing within as well as across individuals, age is automatically quantified and attributed particularly to faces, i.e. more precisely than for any other object. We suggest that processing this quantitative feature, the neural classifier operates on accumulation principles that represent facial age in terms of growing quantities and contrastable numerical magnitudes. By utilizing the ventral part of Wernicke's perpendicular fasciculus, a largely forgotten association tract, age-responsive pITS gains access to pANG, posterior temporal processing core of a common quantification network outlined in a theory of magnitude (ATOM) [**119**] and part of an approximate number system (ANS) [**120**]. Evolutionarily, the object-unselective association area of the angular gyrus constitutes a new formation of

human phylogenesis [**114, 115**] that myelinates late during ontogenetic development [**127**]. Considering the extraordinary relevance of age assessments for the interpersonal domain, e.g. to establish peer communication, attractiveness and even empathy, the cognitive processing of facial age and aging reflects an intrinsic core capacity of the human "social brain".

Sparse data from brain-lesioned patients [**128**] indicate that the posterior right brain may be crucial for the (ap-)perceptive component of age processing. For pANG, such lesions fall into the territory of the middle cerebral artery whereas pITS can also be affected within the border zone to the posterior cerebral artery [**111**]. As yet, we are not aware of any reported cases of pure age and / or gender agnosia which may also indicate their bilateral representation. Increased left-hemispheric responses (see **Figures 3.1**, **3.2** and **3.3**) and higher activations of more accurate raters above the superior temporal sulcus within left pANG only (**Figure 3.4**) correspond with a known importance of the left angular gyrus for abstract number representations, quantized discrete decoding, numerical comparisons and operations [**129, 130**] as well as high mental calculation abilities [**131**]. Given the intrinsic complexities of such representations and their interactions [**132**], future investigations and lesion studies are clearly needed to elucidate cognitive age processing. For example, our analysis may be broadened by other approaches further examining distributed patterns of neural age-encoding in their selectiveness and specificity [**14, 133, 134**] but this would have been beyond the scope of our pilot study. More elaborate insights can be anticipated investigating age discrimination upon face inversion, processing the age of non-face objects, adaptation to age, own- vs. other-age effects including the

associated visual processing strategies and their potential center-periphery bias at simultaneous presentation, cross-modal integration of age-information, age processing in the blind, dissociation of non-abstract and numerical age representations, and the development of age recognition expertise, for instance.

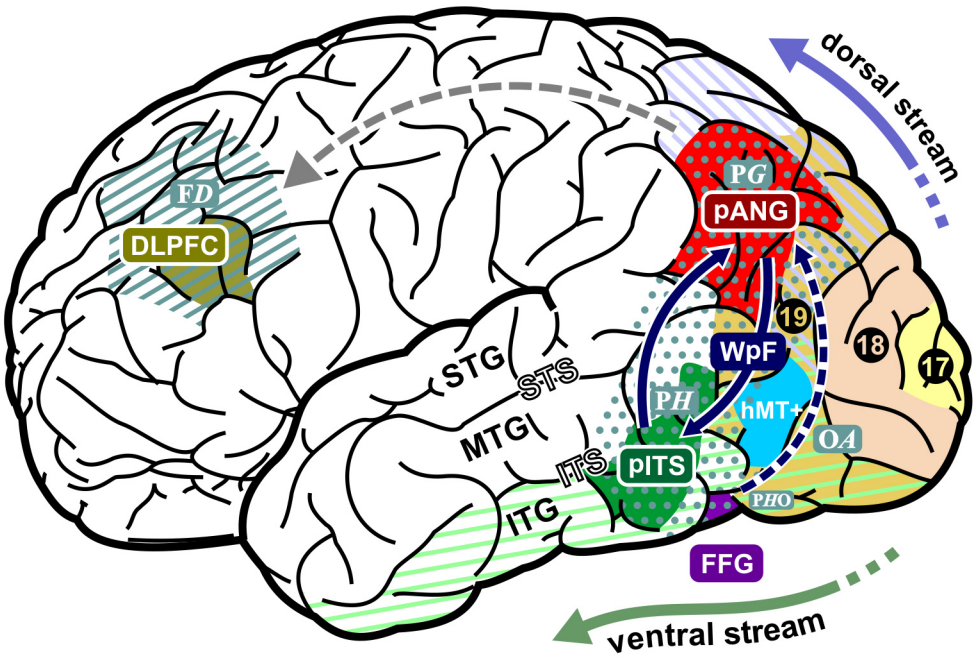

Figure 4.1: Schematic illustration of the age-processing network

Based on a famous sketch of the left hemisphere of the human brain [**135**] age-, gender- and motion-related activations are depicted along with von Economo [**114**] areas to demonstrate the fact that von Economo considered P*H* (area basalis parietalis) to belong to the parietal instead of the temporal lobe. FFG exhibits some connectivity to pANG but is primarily engaged in processing fixed face attributes such as categorical gender (even if continuously changed over different androgyny levels like in **Figure 2.2**).

pANG, posterior angular gyrus area; pITS, posterior inferior temporal sulcus; DLPFC, dorsolateral prefrontal cortex; LOT, lateral occipitotemporal area; FFG, fusiform gyrus; 17-19, Brodmann's areas forming three visual tiers; hMT+, human motion-sensitive temporal cortex; ITG/MTG/STG, inferior/middle/superior temporal gyrus; ITS/STS, inferior/superior temporal sulcus; F*D*, P*G*, P*H*, P*HO* and O*A* von Economo's areas

(Also see **Results**, **Figure 3.8** for a 3D model of the network.)

The notion of a distributed neural core system processing fixed attributes vs. changeable aspects of faces [**30, 31**] parallels the traditional logic of distinguishing essential vs. nonessential object properties which goes back to traditional philosophy. In that regards, facial age may be considered auxiliary appearance, conveying non-symbolic, abstract as well as social information. Like gender and identity, however, age must not constantly be ascertained in another's face and is not reproduced or "mirrored" by the perceiver. Therefore, its regular processing presumably relies less on the constant monitoring mechanisms required to follow eye gaze, lip speech or facial expressions, for example [**31**]. Thus, our results can be interpreted to discover a genuine set in the face processing ensemble that is occupied with age, the posterior inferior sulcus and angular gyrus area. Additionally, the novel demonstration of a particular association between functional and probabilistic connectivity measures and our proposed approach to its assessment may extend the present understanding of relations between fMRI activations and cerebral connectivity.

4.4. Limitations

In addition to pANG and pITS *within* the age-change condition of both hemispheres, significant positive but relatively low vertex-wise spatial cross-correlations of activation probabilities and connectivity values were only found in the right hemisphere for the pANG and LOT clusters on both tractography seeding ends and for both samples (**Figure 3.7**). This relatively weak but significant association of activation probabilities and probabilistic connectivities across the age and gender condition for right pANG and LOT is confounded by the fact that LOT is located close to pITS. Due to

the inherent smoothness of fMRI data, which is pronounced on the average surface, and because connectivity tends to increase the closer seed and target are located, results for short association fibers and cortical regions located so near to each other may be biased. In fact, uncorrected for multiple comparisons the right age-related pITS activation extends into the ipsilateral gender-related LOT cluster which may suggest that right LOT, to some extent, participates in age processing.

Among other potential reasons, this could explain why, to the best of our knowledge, no cases of dissociated impairments in facial age and gender judgments have been reported so far. Nonetheless, such dissociation seems conceivable and should be systematically tested for in brain-lesioned patients even without prosopagnosia, i.e. identification failure of familiar faces. Similarly, connectivity of gender-responsive FFG to nearby pITS and to dorsal pANG may also be relevant for facial age processing (**Figures 3.6** and **3.7**) and support putative but not yet proven age-by-gender interactions if instantiated at the functional level (see further discussion below).

4.4.1. Group-level vs. individual region-of-interest approach

In general, the activations shown are certainly not claimed to be condition-specific and our analysis is a priori limited to functional activations and connectivities of sufficient inter-individual consistency with regards to their anatomical location on the average surface. A range of related problems potentially arising in group studies has been exemplified [**136**] but FreeSurfer's recent boundary- and surface-based intra- [**77**] and inter-individual [**78**] registrations and the reconstruction of individual gray / white

matter boundary surfaces (see **Introduction**, **Figure 1.3** and **Materials and Methods**) may attenuate at least some of these issues. Given that age-responsive functional regions-of-interest (ROI) had not yet been identified before and to enhance the sensitivity and unbiased generalizability of our analysis beyond the single-subject level, we decided not to restrict our analysis to certain areas.

In particular, we did not attempt to illustrate the range of inter-individual and spatial variability in age encoding but the consistency of processing the age of faces in the human brain (**Figures 3.1** and **3.2**), including the association of supreme age-rating competence and age-related activations (**Table 3.2** and **Figure 3.4**). Instead, we tested at the group level on FreeSurfer's average surface for the effects studied. This may, admittedly, uncover only parts of the picture.

4.4.2. Androgyny levels and gender transitions

Additionally, we do recognize that prepuberal faces tend to appear less gendered the younger they are and that very old faces, especially when seen without hairstyle, may be liable to a male classification bias. Therefore, faces of an unambiguous gender were chosen, even for the prepuberal cases that preserved juvenile facial features despite low androgyny levels. The fact that we did not detect a gender-by-age interaction may therefore be related to our specific modeling approach (see **Materials and Methods,** especially **Figure 2.5**) and our stimulus set of clearly gendered faces. The latter limited high androgyny levels to morphs with gender transitions and thereby the power to detect such interaction.

4.4.3. Description and tracking of Wernicke's perpendicular fasciculus

Wernicke's perpendicular fasciculus, whose ventral portion is, according to our results, associated with age processing, has anatomically been recognized as a separate cerebral association tract [**137, 138**]. Because it is embedded into dense white matter pathways of close proximity and crossing fibers, a fact that has been pointed out early for this tract [**139, 140**], Wernicke's perpendicular fasciculus seems to have so far largely escaped further description and attention. Only its more posterior occipital portion has been implied as part of a disconnection syndrome potentially underlying some cases of pure alexia [**141**]. Even though discernible in his excellent sectional brain atlas [**142**], Wernicke's perpendicular fasciculus is not delineated by most of the current references [**143-145**] which is in part due to its superficial but yet poorly defined extension and the cortical variability of the areas connected by its fibers [**146**], including the lower parietal and posterior temporal lobe as well as the FFG [**112**].

In fact, modeling multiple fiber orientations (as performed here by *bedpostx* / *probtrackx*; see **Materials and Methods**) and seeding from gray / white matter surface labels obtained from spherical averaging (using FreeSurfer; see **Introduction**, **Materials and Methods**) was instrumental to its successful tracking. Compared to other association tracts, it runs in a peculiar vertical (instead of horizontal, posterior-anteriorly oriented) course. Especially if pITS and FFG of the occipitotemporal transition are ascribed to the parietal lobe, like von Economo insisted (see legend to **Table 3.3** and **Figure 4.1**), Wernicke's perpendicular fasciculus also exemplifies the debated presence of vertical intralobar autochthonous pathways argued to be of yet

underestimated significance as these connect ventral and more dorsal areas and the corresponding parallel processing pathways [**147**] (see also **Figures 3.8** and **4.1**). Of course, our data cannot exhaustively resolve these issues and remain largely descriptive at this point.

4.4.4. Direction of information processing

Given that tractography itself does not reveal the direction of information processing, our data do not ensure that it is in fact pITS that recruits pANG and not vice versa. The continuous nature of our morphing paradigm, despite its strength of presumably augmenting change-sensitive neural responses and supporting our explicit psychophysiological model, precludes demonstration of temporal delay differences between pITS and pANG without further problematic or clearly violated assumptions. Thus, we acknowledge that the clusters may influence each other reciprocally (as schematically indicated in **Figures 3.8** and **4.1**) – a fact that is generally assumed for most cortical areas connected by association tracts. Actually, unidirectional spatial cross-correlations, i.e. associations of activation probability and connectivity from one cluster to the other but not vice versa, are not straightforward to interpret but minimum intersection maps may reveal focal areas of high connectivity coinciding with activation peaks (as for left posterior pANG activations and connectivity to left FFG; see **Figure 3.6**).

IV. Abbreviations

2D	two dimensional
3D	three dimensional
a (label)	anterior
a.u.	arbitrary units
avg	average
ANOVA	analysis of variance
ANS	Approximate Number System
ATOM	A Theory Of Magnitude
b	b-value (diffusion weighting)
BA	Brodmann area
BET	Brain Extraction Tool
BOLD	blood oxygenation level dependent
COPE	contrast of parameter estimate
cs	connecting samples
CWP	cluster-wise probability
DLPFC	dorsolateral prefrontal cortex
DWI	diffusion weighted imaging
EPI	echo planar imaging
FA	flip angel
FDT	FMRIB's Diffusion Toolbox
FEAT	FMRI Expert Analysis Tool
FFA	fusiform face area
FFG	fusiform gyrus
FILM	FMRIB's Improved Linear Model
FLAIR	fluid-attenuated inversion-recovery
fMRI / FMRI	functional magnetic resonance imaging
FMRIB	Oxford Centre for Functional MRI of the Brain
fps	frames per second

FSL	FMRIB Software Library
FUGUE	FMRIB's Utility for Geometrically Unwarping EPIs
FWER	family-wise error rate
FWHM	full-width-half-maximum
GLM	General Linear Model
hemi	hemisphere
hMT+	human motion sensitive temporal cortex
i (label)	inferior
ITS	inferior temporal sulcus
ITG	inferior temporal gyrus
L / l (label)	left
LOT	lateral occipitotemporal area
MCFLIRT	Motion Correction using FMRIB's Linear Image Registration Tool
ME	mixed effects
mm	millimeter
MNI	Montreal Neurological Institute (average brain template MNI305)
MPRAGE	Magnetization Prepared Rapid Acquisition GRE (Gradient Recalled Echo)
MRI	magnetic resonance imaging
ms	millisecond
MTG	middle temporal gyrus
µs	microsecond
n	sample group size
ns	number of samples
p	probability value
p (label)	posterior
pANG	posterior angular gyrus area
PET	positron emission tomography
pITS	posterior inferior temporal sulcus

PRELUDE	Phase Region Expanding Labeller for Unwrapping Discrete Estimates
R / r (label)	right
s (label)	superior
SD	standard deviation
sec	second
SEM	standard error of the mean
STG	superior temporal gyrus
STS	superior temporal sulcus
T1-weighted	longitudinal magnetization recovery time weighted
T2*-weighted	transverse decay time (including magnetic field inhomogeneity effects) weighted
TE	time to echo
TR	time for repetition
VARCOPE	variance of contrast of parameter estimate
vE	von Economo area
Vtx	Vertex
vVS	ventral visual stream
WpF	Wernicke's perpendicular fasciculus

V. References

1. Chao LL, Haxby JV, & Martin A (1999) Attribute-based neural substrates in temporal cortex for perceiving and knowing about objects. *Nat Neurosci* **2**(10): 913-919.

2. Grill-Spector K & Malach R (2004) The human visual cortex. *Annu Rev Neurosci* **27**: 649-677.

3. Op de Beeck HP, Haushofer J, & Kanwisher NG (2008) Interpreting fMRI data: maps, modules and dimensions. *Nat Rev Neurosci* **9**(2): 123-135.

4. Grill-Spector K*, et al.* (1999) Differential processing of objects under various viewing conditions in the human lateral occipital complex. *Neuron* **24**(1): 187-203.

5. Haxby JV*, et al.* (2001) Distributed and overlapping representations of faces and objects in ventral temporal cortex. *Science* **293**(5539): 2425-2430.

6. Spiridon M & Kanwisher N (2002) How distributed is visual category information in human occipito-temporal cortex? An fMRI study. *Neuron* **35**(6): 1157-1165.

7. Yovel G & Kanwisher N (2004) Face perception: domain specific, not process specific. *Neuron* **44**(5): 889-898.

8. Kanwisher N (2006) What's in a Face? *Science* **311**(5761): 617-618.

9. Tsao DY, Freiwald WA, Tootell RBH, & Livingstone MS (2006) A Cortical Region Consisting Entirely of Face-Selective Cells. *Science* **311**(5761): 670-674.

10. Jiang X*, et al.* (2006) Evaluation of a shape-based model of human face discrimination using FMRI and behavioral techniques. *Neuron* **50**(1): 159-172.

11. Grill-Spector K, Sayres R, & Ress D (2006) High-resolution imaging reveals highly selective nonface clusters in the fusiform face area. *Nat Neurosci* **9**(9): 1177-1185.

12. Tootell RB*, et al.* (2008) fMRI mapping of a morphed continuum of 3D shapes within inferior temporal cortex. *Proc Natl Acad Sci U S A* **105**(9): 3605-3609.

13. Tsao DY & Livingstone MS (2008) Mechanisms of face perception. *Annu Rev Neurosci* **31**: 411-437.

14. Weiner KS & Grill-Spector K (2010) Sparsely-distributed organization of face and limb activations in human ventral temporal cortex. *Neuroimage* **52**(4): 1559-1573.

15. Haist F, Lee K, & Stiles J (2010) Individuating Faces and Common Objects Produces Equal Responses in Putative Face Processing Areas in the Ventral Occipitotemporal Cortex. *Frontiers in Human Neuroscience* **4**: 12.

16. Kanwisher N, McDermott J, & Chun MM (1997) The fusiform face area: a module in human extrastriate cortex specialized for face perception. *J Neurosci* **17**(11): 4302-4311.

17. Aguirre GK, Zarahn E, & D'Esposito M (1998) An area within human ventral cortex sensitive to "building" stimuli: evidence and implications. *Neuron* **21**(2): 373-383.

18. Tong F, Nakayama K, Vaughan JT, & Kanwisher N (1998) Binocular rivalry and visual awareness in human extrastriate cortex. *Neuron* **21**(4): 753-759.

19. Haxby JV*, et al.* (1999) The effect of face inversion on activity in human neural systems for face and object perception. *Neuron* **22**(1): 189-199.

20. Gauthier I*, et al.* (2000) The fusiform "face area" is part of a network that processes faces at the individual level. *J Cogn Neurosci* **12**(3): 495-504.

21. Levy I, Hasson U, Avidan G, Hendler T, & Malach R (2001) Center-periphery organization of human object areas. *Nat Neurosci* **4**(5): 533-539.

22. Hasson U, Levy I, Behrmann M, Hendler T, & Malach R (2002) Eccentricity bias as an organizing principle for human high-order object areas. *Neuron* **34**(3): 479-490.

23. Hasson U, Harel M, Levy I, & Malach R (2003) Large-scale mirror-symmetry organization of human occipito-temporal object areas. *Neuron* **37**(6): 1027-1041.

24. Grill-Spector K, Knouf N, & Kanwisher N (2004) The fusiform face area subserves face perception, not generic within-category identification. *Nat Neurosci* **7**(5): 555-562.

25. Downing PE, Jiang Y, Shuman M, & Kanwisher N (2001) A Cortical Area Selective for Visual Processing of the Human Body. *Science* **293**(5539): 2470-2473.

26. Moro V*, et al.* (2008) The neural basis of body form and body action agnosia. *Neuron* **60**(2): 235-246.

27. Orlov T, Makin TR, & Zohary E (2010) Topographic representation of the human body in the occipitotemporal cortex. *Neuron* **68**(3): 586-600.

28. Freeman JB, Rule NO, Adams RB, Jr., & Ambady N (2009) The neural basis of categorical face perception: graded representations of face gender in fusiform and orbitofrontal cortices. *Cereb Cortex* **20**(6): 1314-1322.

29. Hoffman EA & Haxby JV (2000) Distinct representations of eye gaze and identity in the distributed human neural system for face perception. *Nat Neurosci* **3**(1): 80-84.

30. Haxby JV, Hoffman EA, & Gobbini MI (2000) The distributed human neural system for face perception. *Trends Cogn Sci* **4**(6): 223-233.

31. Calder AJ & Young AW (2005) Understanding the recognition of facial identity and facial expression. *Nat Rev Neurosci* **6**(8): 641-651.

32. Cohen Kadosh K, Henson RN, Cohen Kadosh R, Johnson MH, & Dick F (2009) Task-dependent activation of face-sensitive cortex: an fMRI adaptation study. *J Cogn Neurosci* **22**(5): 903-917.

33. George PA & Hole GJ (1998) Recognising the ageing face: the role of age in face processing. *Perception* **27**(9): 1123-1134.

34. Liu J, Harris A, & Kanwisher N (2002) Stages of processing in face perception: an MEG study. *Nat Neurosci* **5**(9): 910-916.

35. Loffler G, Yourganov G, Wilkinson F, & Wilson HR (2005) fMRI evidence for the neural representation of faces. *Nat Neurosci* **8**(10): 1386-1390.

36. Rotshtein P, Henson RN, Treves A, Driver J, & Dolan RJ (2005) Morphing Marilyn into Maggie dissociates physical and identity face representations in the brain. *Nat Neurosci* **8**(1): 107-113.

37. Ng M, Ciaramitaro VM, Anstis S, Boynton GM, & Fine I (2006) Selectivity for the configural cues that identify the gender, ethnicity, and identity of faces in human cortex. *Proc Natl Acad Sci U S A* **103**(51): 19552-19557.

38. Puce A, Allison T, Bentin S, Gore JC, & McCarthy G (1998) Temporal cortex activation in humans viewing eye and mouth movements. *J Neurosci* **18**(6): 2188-2199.

39. Furl N, van Rijsbergen NJ, Treves A, Friston KJ, & Dolan RJ (2007) Experience-dependent coding of facial expression in superior temporal sulcus. *Proc Natl Acad Sci U S A* **104**(33): 13485-13489.

40. Liu J, Harris A, & Kanwisher N (2009) Perception of face parts and face configurations: an FMRI study. *J Cogn Neurosci* **22**(1): 203-211.

41. Hagan CC*, et al.* (2009) MEG demonstrates a supra-additive response to facial and vocal emotion in the right superior temporal sulcus. *Proc Natl Acad Sci U S A* **106**(47): 20010-20015.

42. Ramanathan N, Chellappa R, & Biswas S (2009) Computational methods for modeling facial aging: A survey. *Journal of Visual Languages & Computing* **20**(3): 131-144.

43. Tranel D, Damasio AR, & Damasio H (1988) Intact recognition of facial expression, gender, and age in patients with impaired recognition of face identity. *Neurology* **38**(5): 690-696.

44. McNeil JE & Warrington EK (1991) Prosopagnosia: a reclassification. *Q J Exp Psychol A* **43**(2): 267-287.

45. McGraw KO, Durm MW, & Durnam MR (1989) The relative salience of sex, race, age, and glasses in children's social perception. *J Genet Psychol* **150**(3): 251-267.

46. O'Craven KM, Downing PE, & Kanwisher N (1999) fMRI evidence for objects as the units of attentional selection. *Nature* **401**(6753): 584-587.

47. Cameron J, **Terminator 2: Judgment Day** (1991, Carolco Pictures, USA, France) http://www.imdb.com/title/tt0103064/

48. Hackford T, **The Devil's Advocate** (1997, Warner Bros. Pictures, USA, Germany) http://www.imdb.com/title/tt0118971/

49. Wachowski A & Wachowski L, **The Matrix** (1999, Warner Bros. Pictures, USA, Australia) http://www.imdb.com/title/tt0133093/

50. Landis J, **Michael Jackson: Black or White** (1991, Epic, Pacific Data Images, USA) http://www.imdb.com/title/tt0255006/

51. Leopold DA, O'Toole AJ, Vetter T, & Blanz V (2001) Prototype-referenced shape encoding revealed by high-level aftereffects. *Nat Neurosci* **4**(1): 89-94.

52. Lauterbur PC (1973) Image Formation by Induced Local Interactions: Examples Employing Nuclear Magnetic Resonance. *Nature* **242**(5394): 190-191.

53. Damadian R, Goldsmith M, & Minkoff L (1977) NMR in cancer: XVI. FONAR image of the live human body. *Physiol Chem Phys* **9**(1): 97-100, 108.

54. Ogawa S*, et al.* (1992) Intrinsic signal changes accompanying sensory stimulation: functional brain mapping with magnetic resonance imaging. *Proc Natl Acad Sci U S A* **89**(13): 5951-5955.

55. Logothetis NK, Pauls J, Augath M, Trinath T, & Oeltermann A (2001) Neurophysiological investigation of the basis of the fMRI signal. *Nature* **412**(6843): 150-157.

56. Logothetis NK (2008) What we can do and what we cannot do with fMRI. *Nature* **453**(7197): 869-878.

57. Conturo TE*, et al.* (1999) Tracking neuronal fiber pathways in the living human brain. *Proc Natl Acad Sci U S A* **96**: 10422-10427.

58. Moseley ME*, et al.* (1990) Diffusion-weighted MR imaging of anisotropic water diffusion in cat central nervous system. *Radiology* **176**(2): 439-445.

59. Behrens TE*, et al.* (2003) Non-invasive mapping of connections between human thalamus and cortex using diffusion imaging. *Nat Neurosci* **6**(7): 750-757.

60. Dale AM, Fischl B, & Sereno MI (1999) Cortical surface-based analysis. I. Segmentation and surface reconstruction. *Neuroimage* **9**(2): 179-194.

61. Fischl B, Sereno MI, & Dale AM (1999) Cortical surface-based analysis. II: Inflation, flattening, and a surface-based coordinate system. *Neuroimage* **9**(2): 195-207.

62. Oldfield RC (1971) The assessment and analysis of handedness: The Edinburgh inventory. *Neuropsychologia* **9**(1): 97-113.

63. Teng EL, Lee P-H, Yang K-S, & Chang PC (1979) Lateral preferences for hand, foot and eye, and their lack of association with scholastic achievement, in 4143 Chinese. *Neuropsychologia* **17**(1): 41-48.

64. Blanz V & Vetter T (1999) A morphable model for the synthesis of 3D faces. on *SIGGRAPH* **99**, Proceedings of the 26th International Conference on Computer Graphics and Interactive Techniques in Los Angeles (ACM Press/Addison-Wesley Publishing Co.)

65. FaceGen Modeller **v3.1** (2004, *Singular Inversions Inc.*, Toronto). http://www.facegen.com/

66. 3ds Max **8** (2005, *Autodesk Inc.*, San Rafael). http://www.autodesk.com/

67. MorphMan 2000 **3.0.1.5** (2002, *STOIK Software*, Moscow). http://www.stoik.com/

68. MATLAB **R2007a** (2007, *The MathWorks Inc.*, Natick). http://www.mathworks.com/

69. Cogent 2000 **v125** (2003, *Wellcome Laboratory of Neurobiology*, London). http://www.vislab.ucl.ac.uk/

70. Gallichan D*, et al.* (2010) Addressing a systematic vibration artifact in diffusion-weighted MRI. *Human Brain Mapping* **31**(2): 193-202.

71. FSL **4.1** (2008, *FMRIB Centre*, Oxford). http://www.fmrib.ox.ac.uk/fsl/

72. FreeSurfer **v4.5.0** (2009, *Martinos Center for Biomedical Imaging*, Charlestown). http://surfer.nmr.mgh.harvard.edu/

73. Jenkinson M, Bannister P, Brady M, & Smith S (2002) Improved optimization for the robust and accurate linear registration and motion correction of brain images. *Neuroimage* **17**(2): 825-841.

74. Smith SM (2002) Fast robust automated brain extraction. *Hum Brain Mapp* **17**(3): 143-155.

75. Woolrich MW, Ripley BD, Brady M, & Smith SM (2001) Temporal autocorrelation in univariate linear modeling of FMRI data. *Neuroimage* **14**(6): 1370-1386.

76. Friston KJ, Worsley KJ, Frackowiak RSJ, Mazziotta JC, & Evans AC (1993) Assessing the significance of focal activations using their spatial extent. *Human Brain Mapping* **1**(3): 210-220.

77. Greve DN & Fischl B (2009) Accurate and robust brain image alignment using boundary-based registration. *Neuroimage* **48**(1): 63-72.

78. Fischl B, Sereno MI, Tootell RB, & Dale AM (1999) High-resolution intersubject averaging and a coordinate system for the cortical surface. *Hum Brain Mapp* **8**(4): 272-284.

79. Beckmann CF, Jenkinson M, & Smith SM (2003) General multilevel linear modeling for group analysis in FMRI. *Neuroimage* **20**(2): 1052-1063.

80. Nichols TE & Holmes AP (2002) Nonparametric permutation tests for functional neuroimaging: a primer with examples. *Hum Brain Mapp* **15**(1): 1-25.

81. Hayasaka S & Nichols TE (2003) Validating cluster size inference: random field and permutation methods. *Neuroimage* **20**(4): 2343-2356.

82. Hayasaka S & Nichols TE (2004) Combining voxel intensity and cluster extent with permutation test framework. *Neuroimage* **23**(1): 54-63.

83. Ernst DM (2004) Permutation Methods: A Basis for Exact Inference. *Statistical Science* **19**(4): 676 - 685.

84. Hagler DJ, Jr., Saygin AP, & Sereno MI (2006) Smoothing and cluster thresholding for cortical surface-based group analysis of fMRI data. *Neuroimage* **33**(4): 1093-1103.

85. Ebner NC (2008) Age of face matters: age-group differences in ratings of young and old faces. *Behav Res Methods* **40**(1): 130-136.

86. Stevens SS (1957) On the psychophysical law. *Psychological Review* **64**(3): 153-181.

87. Ziehen T (1906) *Leitfaden der physiologischen Psychologie in 15 Vorlesungen* (Fischer, **Jena**); pp. 40-45.

88. George PA & Hole GJ (1998) The influence of feature-based information in the age processing of unfamiliar faces. *Perception* **27**(3): 295-312.

89. Ramanathan N & Chellappa R (2006) Face verification across age progression. *IEEE Trans Image Process* **15**(11): 3349-3361.

90. Park U, Tong Y, & Jain AK (2010) Age-invariant face recognition. *IEEE Trans Pattern Anal Mach Intell* **32**(5): 947-954.

91. Barron JL, Fleet DJ, & Beauchemin SS (1994) Performance of optical flow techniques. *International Journal of Computer Vision* **12**(1): 43-77.

92. Simulink **V6.6** (2007, *The MathWorks Inc.*, Natick). http://www.mathworks.com/products/simulink/

93. Horn BKP & Schunck BG (1981) Determining optical flow. *Artificial Intelligence* **17**(1-3): 185-203.

94. Van Essen DC (2004) Organization of Visual Areas in Macaque and Human Cerebral Cortex. ***The Visual Neurosciences***, eds Chalupa L & Werner J (MIT Press, Boston), pp. 507-521.

95. Van Essen DC (2005) A Population-Average, Landmark- and Surface-based (PALS) atlas of human cerebral cortex. *Neuroimage* **28**(3): 635-662.

96. Tootell RB*, et al.* (1998) The retinotopy of visual spatial attention. *Neuron* **21**(6): 1409-1422.

97. Tootell RB*, et al.* (1998) Functional analysis of primary visual cortex (V1) in humans. *Proc Natl Acad Sci U S A* **95**(3): 811-817.

98. Hadjikhani N, Liu AK, Dale AM, Cavanagh P, & Tootell RB (1998) Retinotopy and color sensitivity in human visual cortical area V8. *Nat Neurosci* **1**(3): 235-241.

99. Somers DC, Dale AM, Seiffert AE, & Tootell RB (1999) Functional MRI reveals spatially specific attentional modulation in human primary visual cortex. *Proc Natl Acad Sci U S A* **96**(4): 1663-1668.

100. Tootell RB & Hadjikhani N (2001) Where is 'dorsal V4' in human visual cortex? Retinotopic, topographic and functional evidence. *Cereb Cortex* **11**(4): 298-311.

101. Van Essen DC & Dierker DL (2007) Surface-based and probabilistic atlases of primate cerebral cortex. *Neuron* **56**(2): 209-225.

102. Behrens TE, Berg HJ, Jbabdi S, Rushworth MF, & Woolrich MW (2007) Probabilistic diffusion tractography with multiple fibre orientations: What can we gain? *Neuroimage* **34**(1): 144-155.

103. Swain MJ & Ballard DH (1991) Color indexing. *Int. J. Comput. Vision* **7**(1): 11-32.

104. Sergent J, Ohta S, & MacDonald B (1992) Functional neuroanatomy of face and object processing. A positron emission tomography study. *Brain* **115 Pt 1**: 15-36.

105. Zeki S*, et al.* (1991) A direct demonstration of functional specialization in human visual cortex. *J Neurosci* **11**(3): 641-649.

106. Tootell RB*, et al.* (1995) Functional analysis of human MT and related visual cortical areas using magnetic resonance imaging. *J Neurosci* **15**(4): 3215-3230.

107. Morrone MC*, et al.* (2000) A cortical area that responds specifically to optic flow, revealed by fMRI. *Nat Neurosci* **3**(12): 1322-1328.

108. Vanduffel W*, et al.* (2002) Extracting 3D from motion: differences in human and monkey intraparietal cortex. *Science* **298**(5592): 413-415.

109. DeAngelis GC, Cumming BG, & Newsome WT (1998) Cortical area MT and the perception of stereoscopic depth. *Nature* **394**(6694): 677-680.

110. Dejerine J & Dejerine-Klumpke AM (1895) *Anatomie des centres nerveux* (Rueff & Cie., **Paris**); p. 757.

111. Duvernoy HM (1999) *The human brain. Surface, blood supply, and three-dimensional sectional anatomy* (Springer, **Wien**); pp. 6, 13, 394-397, 463-473.

112. Retzius G (1896) *Das Menschenhirn Vol. I* (Norstedt, **Stockholm**); pp. 124-142.

113. Noback CR & Demarest RJ (1975) *The human nervous system: basic principles of neurobiology.* (McGraw-Hill, **New York**); p. 451.

114. von Economo C (1927) *Zellaufbau der Grosshirnrinde des Menschen* (Springer, **Berlin**); pp. 2-78, 84-107.

115. Brodmann K (1909) *Vergleichende Lokalisationslehre der Großhirnrinde in ihren Prinzipien dargestellt auf Grund des Zellenbaues* (J. A. Barth, **Leipzig**); pp. 131-143, 230.

116. Ross J (1883) Reviews and notices of books - Lehrbuch der Gehirnkrankheiten für Aerzte und Studierende. Von Dr. C. Wernicke. 3 vols. Fischer, Kassel, 1881-1883. (see vol. 1, p. 23). *Brain* **6**(3): 398-403.

117. Wernicke C (1877) XX. Sitzung am 12. Januar 1877. *Verhandlungen der Physiologischen Gesellschaft zu Berlin Jahrgang I. und II. (XX. Sitzung am 12. Januar 1877) printed in: Deutsche Medizinische Wochenschrift* **12**(XX. Sitzung am 12. Januar 1877): 2-4.

118. Quain J (1891) *Quain's Elements of anatomy, Vol. III. Part I., The Spinal Cord And Brain* (Longmans, Green and Co., **London**); pp. 165-166.

119. Walsh V (2003) A theory of magnitude: common cortical metrics of time, space and quantity. *Trends Cogn Sci* **7**(11): 483-488.

120. Cantlon JF, Platt ML, & Brannon EM (2009) Beyond the number domain. *Trends Cogn Sci* **13**(2): 83-91.

121. Ebner NC*, et al.* (in press) Medial prefrontal cortex activity when thinking about others depends on their age. *Neurocase* **17**.

122. Ishai A, Ungerleider LG, & Haxby JV (2000) Distributed neural systems for the generation of visual images. *Neuron* **28**(3): 979-990.

123. Druzgal TJ & D'Esposito M (2001) A neural network reflecting decisions about human faces. *Neuron* **32**(5): 947-955.

124. Vuilleumier P, Armony JL, Driver J, & Dolan RJ (2001) Effects of attention and emotion on face processing in the human brain: an event-related fMRI study. *Neuron* **30**(3): 829-841.

125. Aharon I*, et al.* (2001) Beautiful faces have variable reward value: fMRI and behavioral evidence. *Neuron* **32**(3): 537-551.

126. Singer T, Kiebel SJ, Winston JS, Dolan RJ, & Frith CD (2004) Brain responses to the acquired moral status of faces. *Neuron* **41**(4): 653-662.

127. Flechsig P (1901) Developmental (Myelogenetic) Localisation of the Cerebral Cortex in the Human Subject. *Lancet* **158**(4077): 1027-1030.

128. De Renzi E, Bonacini MG, & Faglioni P (1989) Right posterior brain-damaged patients are poor at assessing the age of a face. *Neuropsychologia* **27**(6): 839-848.

129. Göbel S, Walsh V, & Rushworth MFS (2001) The Mental Number Line and the Human Angular Gyrus. *Neuroimage* **14**(6): 1278-1289.

130. Göbel SM, Rushworth MF, & Walsh V (2006) Inferior parietal rTMS affects performance in an addition task. *Cortex* **42**(5): 774-781.

131. Grabner RH*, et al.* (2007) Individual differences in mathematical competence predict parietal brain activation during mental calculation. *Neuroimage* **38**(2): 346-356.

132. Hubbard EM, Piazza M, Pinel P, & Dehaene S (2005) Interactions between number and space in parietal cortex. *Nat Rev Neurosci* **6**(6): 435-448.

133. Courtney SM, Ungerleider LG, Keil K, & Haxby JV (1997) Transient and sustained activity in a distributed neural system for human working memory. *Nature* **386**(6625): 608-611.

134. Hanson SJ & Schmidt A (2011) High-resolution imaging of the fusiform face area (FFA) using multivariate non-linear classifiers shows diagnosticity for non-face categories. *Neuroimage* **54**(2): 1715-1734.

135. Gray H (1918) *Anatomy of the human body, by Henry Gray. 20th ed., thoroughly rev. and re-edited by Warren H. Lewis* (Lea & Febiger, **Philadelphia**); fig. 728.

136. Fedorenko E & Kanwisher N (2009) Neuroimaging of Language: Why Hasn't a Clearer Picture Emerged? *Language and Linguistics Compass* **3**(4): 839-865.

137. Braus H (1932) *Anatomie des Menschen. Ein Lehrbuch für Studierende und Ärzte. Dritter Band, Centrales Nervensystem (von Elze, C.)* (Springer, **Berlin**); pp. 175-176.

138. v. Lanz T & Wachsmuth W (1985) *Praktische Anatomie. Erster Band, erster Teil, Kopf, Teil A, Übergeordnete Systeme (von Lang, J.)* (Springer, **Berlin**); pp. 306-307.

139. Meynert T (1905) *Gehirnpathologie 2. Aufl., Bd. I* (Hölder, **Wien**); pp. 62, 72.

140. Kappers CUA, Huber C, & Crosby E (1967) *The comparative anatomy of the nervous system of vertebrates, including man Vol. III* (Hafner, **New York**); pp. 1470-1471.

141. Greenblatt SH (1973) Alexia without agraphia or hemianopsia. Anatomical analysis of an autopsied case. *Brain* **96**(2): 307-316.

142. Wernicke C (1897) *Photographischer Atlas des Gehirns* (Verlag der Psychiatrischen Klinik der Universität, **Breslau**); Tafel XXVI-XXVIII.

143. Mori S*, et al.* (2002) Imaging cortical association tracts in the human brain using diffusion-tensor-based axonal tracking. *Magn Reson Med* **47**(2): 215-223.

144. Mori S, Wakana S, Nagae-Poetscher LM, & van Zijl PCM (2005) *MRI atlas of human white matter* (Elsevier, **Amsterdam**); pp. 23-29.

145. Hua K*, et al.* (2009) Mapping of functional areas in the human cortex based on connectivity through association fibers. *Cereb Cortex* **19**(8): 1889-1895.

146. Oishi K*, et al.* (2008) Human brain white matter atlas: Identification and assignment of common anatomical structures in superficial white matter. *Neuroimage* **43**(3): 447-457.

147. ffytche DH & Catani M (2005) Beyond localization: from hodology to function. *Philosophical Transactions of the Royal Society B: Biological Sciences* **360**(1456): 767-779.

VI. Appendix

VI.I. Maintaining color balance

The following iterative Matlab script was used to keep the color balance of the displayed paradigm constant. This involved adapting of color, luminance, gamma and contrast levels of every frame. (The script here is customized for the example morphing sequence with black background and the characteristics of the presentation display):

```
% Adjust Color Channel Contrast & Luminance %
 function [msg] = CoLumCorvL3 (filename, outname)

for loopframes = 1:24:145 % Loop Keyframe Filename

filenumber = loopframes - 1;
filenamenum = num2str(filenumber);
filename1 = ([filename ,'0', filenamenum, '.png']);
if filenumber < 100
  filename1 = ([filename ,'00', filenamenum, '.png']);
end
if filenumber < 10
  filename1 = ([filename ,'000', filenamenum, '.png']);
end

Frame = imread(filename1);

factori = 0.0001;
factorg = 0.0001;

% for cycle = 1:3 <- unnecessary extra iteration for precise adjustment

cycle = 1;

% change Color Channels
replow = 0;
rephi = 0;
lowin = 0;
hiwin = 1;
gammaG = 1;
colorRGB = squeeze(mean(mean(Frame)));
colorRGB2 = colorRGB;
FrameC = Frame;

if colorRGB(1,1) < 75.0
while colorRGB2(1,1) < 75.0 && colorRGB2(1,1) ~= 75.0
   gammaG = gammaG-factorg;
   rephi = rephi+1;
   hiwin = hiwin-factori;
   FrameC(:,:,1) = imadjust(Frame(:,:,1), [0; hiwin], [0; 1],gammaG);
   colorRGB2 = squeeze(mean(mean(FrameC)));
```

```
end
else
while colorRGB2(1,1) > 75.0 && colorRGB2(1,1) ~= 75.0
   gammaG = gammaG+factorg;
   replow = replow-1;
   lowin = lowin+factori;
   FrameC(:,:,1) = imadjust(Frame(:,:,1), [lowin; 1], [0; 1],gammaG);
   colorRGB2 = squeeze(mean(mean(FrameC)));
end
end

Frame = FrameC;
chtable(cycle,1,loopframes) = lowin;
chtable(cycle,2,loopframes) = hiwin;
chtable(cycle,3,loopframes) = gammaG;

replow = 0;
rephi = 0;
lowin = 0;
hiwin = 1;
gammaG = 1;

if colorRGB(2,1) < 59.0
while colorRGB2(2,1) < 59.0 && colorRGB2(2,1) ~= 59.0
   gammaG = gammaG-factorg;
   rephi = rephi+1;
   hiwin = hiwin-factori;
   FrameC(:,:,2) = imadjust(Frame(:,:,2), [0; hiwin], [0; 1],gammaG);
   colorRGB2 = squeeze(mean(mean(FrameC)));
end
else
while colorRGB2(2,1) > 59.0 && colorRGB2(2,1) ~= 59.0
   gammaG = gammaG+factorg;
   replow = replow-1;
   lowin = lowin+factori;
   FrameC(:,:,2) = imadjust(Frame(:,:,2), [lowin; 1], [0; 1],gammaG);
   colorRGB2 = squeeze(mean(mean(FrameC)));
end
end

Frame = FrameC;
chtable(cycle,4,loopframes) = lowin;
chtable(cycle,5,loopframes) = hiwin;
chtable(cycle,6,loopframes) = gammaG;

replow = 0;
rephi = 0;
lowin = 0;
hiwin = 1;
gammaG = 1;

if colorRGB(3,1) < 50.0
while colorRGB2(3,1) < 50.0 && colorRGB2(3,1) ~= 50.0
   gammaG = gammaG-factorg;
   rephi = rephi+1;
   hiwin = hiwin-factori;
```

```
   FrameC(:,:,3) = imadjust(Frame(:,:,3), [0; hiwin], [0; 1],gammaG);
   colorRGB2 = squeeze(mean(mean(FrameC)));
end
else
while colorRGB2(3,1) > 50.0 && colorRGB2(3,1) ~= 50.0
   gammaG = gammaG+factorg;
   replow = replow-1;
   lowin = lowin+factori;
   FrameC(:,:,3) = imadjust(Frame(:,:,3), [lowin; 1], [0; 1],gammaG);
   colorRGB2 = squeeze(mean(mean(FrameC)));
end
end

Frame = FrameC;
chtable(cycle,7,loopframes) = lowin;
chtable(cycle,8,loopframes) = hiwin;
chtable(cycle,9,loopframes) = gammaG;

% change Contrast
FrameX = changem(Frame, [255 255], [0 1]);
LH1 = stretchlim(FrameX, [0.005 0.995]);
LH2 = stretchlim(Frame, [0.005 0.995]);
minLH = min(min(LH1));
maxLH = max(max(LH2));

Frame = imadjust(Frame, [minLH minLH minLH; maxLH maxLH maxLH], [0 0 0; 1 1 1],1);

chtable(cycle,10,loopframes) = minLH;
chtable(cycle,11,loopframes) = maxLH;

% correct distribution
f1 = 75.0/59.0;
f2 = 50.0/59.0;

cycle = 2;

replow = 0;
rephi = 0;
lowin = 0;
lowin2 = lowin;
factorii = factori;
hiwin = 1;
hiwin2 = hiwin;
gammaG = 1;
colorRGB = squeeze(mean(mean(Frame)));
colorRGB2 = colorRGB;
FrameC = Frame;

if colorRGB(1,1) < colorRGB(2,1)*f1
while colorRGB2(1,1) < colorRGB(2,1)*f1 && colorRGB2(1,1) ~= colorRGB(2,1)*f1
   gammaG = gammaG-factorg;
   rephi = rephi+1;
   factorii = factorii+factori;
   hiwin2 = hiwin-factorii;
   FrameC(:,:,1) = imadjust(Frame(:,:,1), [0; hiwin2], [0; 1],gammaG);
   colorRGB2 = squeeze(mean(mean(FrameC)));
```

```
end
   hiwin2 = hiwin-(factorii/2);
   FrameC(:,:,1) = imadjust(Frame(:,:,1), [0; hiwin2], [0; 1],gammaG);
else
while colorRGB2(1,1) > colorRGB(2,1)*f1 && colorRGB2(1,1) ~= colorRGB(2,1)*f1
   gammaG = gammaG+factorg;
   replow = replow-1;
   factorii = factorii+factori;
   lowin2 = lowin+factorii;
   FrameC(:,:,1) = imadjust(Frame(:,:,1), [lowin2; 1], [0; 1],gammaG);
   colorRGB2 = squeeze(mean(mean(FrameC)));
end
   lowin2 = lowin+(factorii/2);
   FrameC(:,:,1) = imadjust(Frame(:,:,1), [lowin2; 1], [0; 1],gammaG);
end

Frame = FrameC;
chtable(cycle,1,loopframes) = lowin2;
chtable(cycle,2,loopframes) = hiwin2;
chtable(cycle,3,loopframes) = gammaG;

replow = 0;
rephi = 0;
factorii = factori;
lowin = 0;
lowin2 = lowin;
hiwin = 1;
hiwin2 = hiwin;
gammaG = 1;

if colorRGB(3,1) < colorRGB(2,1)*f2
while colorRGB2(3,1) < colorRGB(2,1)*f2 && colorRGB2(3,1) ~= colorRGB(2,1)*f2
   gammaG = gammaG-factorg;
   rephi = rephi+1;
   factorii = factorii+factori;
   hiwin2 = hiwin-factorii;
   FrameC(:,:,3) = imadjust(Frame(:,:,3), [0; hiwin2], [0; 1],gammaG);
   colorRGB2 = squeeze(mean(mean(FrameC)));
end
   hiwin2 = hiwin-(factorii/2);
   FrameC(:,:,3) = imadjust(Frame(:,:,3), [0; hiwin2], [0; 1],gammaG);
else
while colorRGB2(3,1) > colorRGB(2,1)*f2 && colorRGB2(3,1) ~= colorRGB(2,1)*f2
   gammaG = gammaG+factorg;
   replow = replow-1;
   factorii = factorii+factori;
   lowin2 = lowin+factorii;
   FrameC(:,:,3) = imadjust(Frame(:,:,3), [lowin2; 1], [0; 1],gammaG);
   colorRGB2 = squeeze(mean(mean(FrameC)));
end
   lowin2 = lowin+(factorii/2);
   FrameC(:,:,3) = imadjust(Frame(:,:,3), [lowin2; 1], [0; 1],gammaG);
end

Frame = FrameC;
chtable(cycle,4,loopframes) = lowin2;
```

```
chtable(cycle,5,loopframes) = hiwin2;
chtable(cycle,6,loopframes) = gammaG;
chtable(:,:,loopframes)    % Display output

% write image
outname1 = ([outname ,'0', filenamenum, '.png']);
if filenumber < 100
  outname1 = ([outname ,'00', filenamenum, '.png']);
end
if filenumber < 10
  outname1 = ([outname ,'000', filenamenum, '.png']);
end
imwrite(Frame,outname1);

loopframes    % Display output

end

% linear interpolation of keyframe correction to reduce computing time and eliminate color jitter %

for loopframes = 2:144 % Loop Keyframe Filename

if loopframes == 25 || loopframes == 49 || loopframes == 73 || loopframes == 97 || loopframes == 121
   continue
end

filenumber = loopframes - 1;

filenamenum = num2str(filenumber);

filename1 = ([filename ,'0', filenamenum, '.png']);
if filenumber < 100
  filename1 = ([filename ,'00', filenamenum, '.png']);
end
if filenumber < 10
  filename1 = ([filename ,'000', filenamenum, '.png']);
end

Frame = imread(filename1);

if loopframes >= 2 && loopframes < 25
   loloop = 1;
   hiloop = 25;
end

if loopframes >= 26 && loopframes < 49
   loloop = 25;
   hiloop = 49;
end

if loopframes >= 50 && loopframes < 73
   loloop = 49;
   hiloop = 73;
end

if loopframes >= 74 && loopframes < 97
```

```
   loloop = 73;
   hiloop = 97;
end

if loopframes >= 98 && loopframes < 121
   loloop = 97;
   hiloop = 121;
end

if loopframes >= 122 && loopframes < 145
   loloop = 121;
   hiloop = 145;
end

chtable(:,:,loopframes) = chtable(:,:,loloop) - ((chtable(:,:,loloop)-chtable(:,:,hiloop)) \
.*((loopframes-loloop)/24));

% change Color Channels
Frame(:,:,1) = imadjust(Frame(:,:,1), [chtable(1,1,loopframes) ; chtable(1,2,loopframes)], [0; 1], \
chtable(1,3,loopframes));
Frame(:,:,2) = imadjust(Frame(:,:,2), [chtable(1,4,loopframes) ; chtable(1,5,loopframes)], [0; 1], \
chtable(1,6,loopframes));
Frame(:,:,3) = imadjust(Frame(:,:,3), [chtable(1,7,loopframes) ; chtable(1,8,loopframes)], [0; 1], \
chtable(1,9,loopframes));

% change Contrast
Frame = imadjust(Frame, [chtable(1,10,loopframes) chtable(1,10,loopframes) \
chtable(1,10,loopframes); chtable(1,11,loopframes) chtable(1,11,loopframes) \
chtable(1,11,loopframes)], [0 0 0; 1 1 1],1);

% correct distribution
Frame(:,:,1) = imadjust(Frame(:,:,1), [chtable(2,1,loopframes) ; chtable(2,2,loopframes)], \
[0; 1],chtable(2,3,loopframes));
Frame(:,:,3) = imadjust(Frame(:,:,3), [chtable(2,4,loopframes) ; chtable(2,5,loopframes)], \
[0; 1],chtable(2,6,loopframes));
chtable(:,:,loopframes)    % Display output

% write image
outname1 = ([outname ,'0', filenamenum, '.png']);
if filenumber < 100
  outname1 = ([outname ,'00', filenamenum, '.png']);
end
if filenumber < 10
  outname1 = ([outname ,'000', filenamenum, '.png']);
end
imwrite(Frame,outname1);

loopframes    % Display output

end

msg = 'ok';
```

VI.II. Exemplary morph sequence

The exemplary morph video (ExpFaceMorph) is available in Windows AVI and Apple QuickTime format for download here:

http://www.neuroradiologie.uni-wuerzburg.de/HomolaDiss/

VII. List of Publications

P1. Bartsch AJ, Homola G, Biller A, Solymosi L, & Bendszus M (2006) Diagnostic functional MRI: illustrated clinical applications and decision-making. *J Magn Reson Imaging* **23**(6): 921-932.

P2. Bartsch AJ, Homola G, Biller A, Smith SM, Weijers HG, Wiesbeck GA, Jenkinson M, De Stefano N, Solymosi L, & Bendszus M (2007) Manifestations of early brain recovery associated with abstinence from alcoholism. *Brain* **130**(Pt 1): 36-47.

P3. Bartsch AJ, Homola G, Thesen S, Sahmer P, Keim R, Beckmann CF, Biller A, Knaus C, & Bendszus M (2007) Scanning for the scanner: FMRI of audition by read-out omissions from echo-planar imaging. *Neuroimage* **35**(1): 234-243.

P4. Haller S, Homola GA, Scheffler K, Beckmann CF, & Bartsch AJ (2009) Background MR gradient noise and non-auditory BOLD activations: a data-driven perspective. *Brain Res* **1282**: 74-83.

P5. Biller A, Bartsch AJ, Homola G, Solymosi L, & Bendszus M (2009) The effect of ethanol on human brain metabolites longitudinally characterized by proton MR spectroscopy. *J Cereb Blood Flow Metab* **29**(5): 891-902.

P6. Bartsch AJ, Biller A, & Homola GA (2009) Tractography for Surgical Targeting. ***Diffusion MRI***, eds Johansen-Berg H & Behrens TEJ (Academic Press, San Diego), pp. 415-444.

P7. Jbabdi S, Homola GA, & Bartsch AJ (2010) Structural connectivity between functional activations - a probabilistic link beyond simple "blob" location? Poster Presentation at the *16th Annual Meeting of the Organization for Human Brain Mapping* (**Barcelona**)

P8. Homola GA, Jbabdi S, Beckmann CF, & Bartsch AJ (2011) A Brain Network Processing the Age of Faces. *(submitted)*

VIII. Ehrenwörtliche Erklärung

Erklärung gemäß § 4, Absatz 3 der Promotionsordnung der Fakultät für Biologie der Bayerischen Julius-Maximilians-Universität Würzburg vom 15. März 1999 zuletzt geändert durch Satzung vom 12. August 2009

Hiermit erkläre ich, die vorgelegte Dissertation selbstständig angefertigt und keine anderen als die von mir angegeben Quellen und Hilfsmittel benutzt zu haben. Alle aus der Literatur entnommenen Stellen sind als solche kenntlich gemacht.

Des Weiteren erkläre ich, dass die vorliegende Arbeit weder in gleicher noch in ähnlicher Form in einem anderen Prüfungsverfahren vorgelegen hat. Zuvor habe ich keine akademischen Grade erworben oder zu erwerben versucht.

Würzburg, den 20.03.2011 _____

György A. Homola